

MIT Open Access Articles

*Stress#Induced Anomalous Transport
in Natural Fracture Networks*

The MIT Faculty has made this article openly available. **Please share**
how this access benefits you. Your story matters.

Citation: Kang, Peter K. et al. "Stress#Induced Anomalous Transport in Natural Fracture Networks." *Water Resources Research* 55, 5 (May 2019): 4163-4185 © 2019 American Geophysical Union

As Published: <http://dx.doi.org/10.1029/2019wr024944>

Publisher: American Geophysical Union (AGU)

Persistent URL: <https://hdl.handle.net/1721.1/129664>

Version: Author's final manuscript: final author's manuscript post peer review, without publisher's formatting or copy editing

Terms of use: Creative Commons Attribution-Noncommercial-Share Alike



Stress-induced Anomalous Transport in Natural Fracture Networks¹

Peter K. Kang^{1,2}, Qinghua Lei³, Marco Dentz⁴ and Ruben Juanes⁵

¹Department of Earth Sciences, University of Minnesota, Minneapolis, USA

²Saint Anthony Falls Laboratory, University of Minnesota, Minneapolis, USA

³Department of Earth Sciences, ETH Zurich, Zurich, Switzerland

⁴Institute of Environmental Assessment and Water Research (IDAEA), Spanish National Research Council (CSIC),
Barcelona, Spain

⁵Department of Civil and Environmental Engineering, Massachusetts Institute of Technology, Cambridge, USA

Key Points:

- We investigate the effects of fracture network geometry, aperture heterogeneity, and geological stress on fluid flow and transport
- Geological stress and geomechanical deformation can induce anomalous transport, evidenced by early arrival and late-time tailing
- A Bernoulli CTRW model captures the stress-induced anomalous transport in natural fracture networks

¹ Kang, P., L. Qinghua, M. Dentz, and R. Juanes, Stress-induced Anomalous Transport in Natural Fracture Networks, Water Resour. Res., <https://doi.org/10.1029/2019WR024944>, 2019.

Corresponding author: Peter K. Kang, pkkang@umn.edu

Abstract

We investigate the effects of geological stress on fluid flow and tracer transport in natural fracture networks. We show the emergence of non-Fickian (anomalous) transport from the interplay among fracture network geometry, aperture heterogeneity, and geological stress. In this study, we extract the fracture network geometry from the geological map of an actual rock outcrop, and we simulate the geomechanical behavior of fractured rock using a hybrid finite-discrete element method. We analyze the impact of stress on the aperture distribution, fluid flow field and tracer transport properties. Both stress magnitude and orientation have strong effects on the fracture aperture field, which in turn affects fluid flow and tracer transport through the system. We observe that stress anisotropy may cause significant shear dilation along long, curved fractures that are preferentially oriented to the stress loading. This, in turn, induces preferential flow paths and anomalous early arrival of tracers. An increase in stress magnitude enhances aperture heterogeneity by introducing more small apertures, which exacerbates late-time tailing. This effect is stronger when there is higher heterogeneity in the initial aperture field. To honor the flow field with strong preferential flow paths, we extend the Bernoulli Continuous Time Random Walk model to incorporate dual velocity correlation length scales. The proposed upscaled transport model captures anomalous transport through stressed fracture networks, and agrees quantitatively with the high-fidelity numerical simulations.

1 Introduction

Fractures are ubiquitous in subsurface rocks, and fluid flow and mass transport in fractured media control many important subsurface processes and engineering applications. One attractive way of modeling fractured media is using a discrete fracture network (DFN) approach (Berkowitz & Scher, 1997; Cacas, Ledoux, de Marsily, et al., 1990; Huseby, Thovet, & Adler, 2001; Juanes, Samper, & Molinero, 2002; Koudina, Garcia, Thovet, & Adler, 1998; Molinero, Samper, & Juanes, 2002; Park, de Dreuzy, Lee, & Berkowitz, 2001). DFN models represent fractures as discrete entities and enable the study of the effects of fracture geometrical properties on fluid flow and transport explicitly. Fluid flow and transport in DFNs has been the subject of many investigations over the past decades, and recent advances in computational power have enabled more detailed flow and transport studies in complex three-dimensional (3D) DFNs with multiscale heterogeneity (Benedetto, Berrone, Borio, Pieraccini, & Scialò, 2016; J. Hyman & Jiménez-Martínez, 2018; J. D. Hyman, Dentz, Hagberg, & Kang, 2019; Maillot, Davy, Le Goc, Dar-

cel, & De Dreuzy, 2016; Makedonska, Painter, Bui, Gable, & Karra, 2015; Viswanathan et al., 2018).

Recent studies have shown that the multiscale heterogeneity of fracture media—from single fracture-scale roughness to fracture network-scale heterogeneity—induces anomalous (non-Fickian) transport (Cardenas, Slottke, Ketcham, & Sharp, 2007; Edery, Geiger, & Berkowitz, 2016; Kang, Dentz, Le Borgne, Lee, & Juanes, 2017; Kang, Le Borgne, Dentz, Bour, & Juanes, 2015; L. Wang & Cardenas, 2014). Anomalous transport is widely observed from laboratory experiments in packed beds (Kandhai et al., 2002; Moroni, Kleinfelter, & Cushman, 2007), sand columns (Levy & Berkowitz, 2003) and rock samples (Bijeljic, Mostaghimi, & Blunt, 2011; Kang et al., 2014; Porta, Bijeljic, Blunt, & Guadagnini, 2015; Scheven, Verganelakis, Harris, Johns, & Gladden, 2005) to field scale experiments (Garabedian, LeBlanc, Gelhar, & Celia, 1991; Kang, Le Borgne, et al., 2015; Le Borgne & Gouze, 2007). The key features of anomalous transport are early arrival of tracers, long tailing of tracers, and non-Gaussian plume shapes, and these features cannot be properly captured by a traditional advection-dispersion formulation. Predicting anomalous transport is critically important for various engineering applications including subsurface contaminant transport, geological nuclear waste disposal and carbon sequestration.

Fractures are always subjected to *in-situ* stresses, which can modify fracture network properties. *In-situ* stresses are often variable in space and time as a result of the superposition of far-field stresses and local perturbations. The far-field stresses related to plate-driving forces are typically uniform over the lithospheric scale (Zoback, 1992), while local perturbations may be induced by the presence of geological structures such as fractures (Lei & Gao, 2018), heterogeneity in elastic properties, and changes in pore pressure from fluid injection and extraction. The resulting spatially-variable stress field may lead to a heterogeneous distribution of fracture apertures due to the strong dependence of fracture deformation on normal/shear loadings (Bandis, Lumsden, & Barton, 1983; N. Barton, Bandis, & Bakhtar, 1985). Starting from the seminal work by Witherspoon, Wang, Iwai, and Gale (1980), great efforts have been devoted to investigating the coupled effects between stress and fluid flow in fractured rocks (Baghbanan & Jing, 2008; Figueiredo, Tsang, Rutqvist, & Niemi, 2015; Latham et al., 2013; Lei, Latham, & Tsang, 2017; Liu, Li, Jiang, & Yu, 2018; Ma, Wang, Li, & Chen, 2019; Min, Rutqvist, Tsang, & Jing, 2004; Oda, 1986; Pyrak-Nolte & Morris, 2000; Raven & Gale, 1985; Rutqvist & Stephansson, 2003; Zhang & Sanderson, 1996). The permeability tensor was observed to

be highly sensitive to both fracture network properties (e.g., aperture, length, density, and orientation) and the *in-situ* stress conditions (e.g., magnitude and direction).

A few recent studies have investigated the role of stress on solute transport in fracture networks (Jing, Min, Baghbanan, & Zhao, 2013; Nick, Paluszny, Blunt, & Matthäi, 2011; Rutqvist, Leung, Hoch, Wang, & Wang, 2013; Z. Wang et al., 2014; Zhao, Jing, & Neretnieks, 2010; Zhao, Jing, Neretnieks, & Moreno, 2011; Zhao et al., 2013), and have shown that geological stress can be a key determinant for the transport of solutes. These effects were investigated systematically for the first time by Zhao et al. (2011). They found that, for fracture networks with constant initial apertures and under moderate stress anisotropy, an increase in stress magnitude leads to a delay in solute arrival times, whereas, at higher stress anisotropy, shear can give rise to preferential flow paths by dilating fractures, thereby leading to early arrival of solutes. These previous studies analyze stress effects on solute transport on the basis of tracer breakthrough curves and tracer mean arrival times. Moreover, the role of heterogeneity in the initial aperture remains unexplored. This limits our fundamental understanding of the links among stress, fracture network geometry, fracture aperture distribution, flow and transport—something that we address here for the first time. Through high-fidelity numerical modeling of fluid flow and transport through stressed fracture networks, we show that geological stress can induce anomalous transport in fracture networks, and we elucidate the underlying mechanisms responsible for this behavior. We also propose a parsimonious upscaled model that can capture anomalous transport through *stressed* fracture networks for the first time.

In a recent study, we have shown that confining stress can lead to anomalous transport in single rough fractures (Kang, Brown, & Juanes, 2016), but an analysis of the impact of stress on anomalous transport at the fracture-network scale is still lacking. Here, we extend the study of stress effects on anomalous transport to the fracture-network scale, which is critical for improving our fundamental understanding of subsurface processes and for quantitative assessments in many subsurface engineering applications (C.-F. Tsang, 1991).

We conduct our analysis on a two-dimensional fracture network obtained from the mapping of an actual outcrop. To study the effects of aperture variability, we consider two different initial settings, with either constant or variable initial aperture field. We then perform numerical modeling of geomechanics under different stress magnitudes and orientations, and model flow and tracer transport in stressed DFNs to address the effects of varying stress on anomalous transport. To focus on stress effects on fracture flow and transport, we do not consider

matrix diffusion in this study. Finally, we develop a parsimonious upscaled transport model based on the analysis of Lagrangian velocity statistics.

2 Methodology

2.1 Natural fracture network

The natural fracture network used in this study is based on a limestone outcrop (18 m \times 8 m) located at the southern margin of the Bristol Channel Basin, UK (Figure 1) (Belayneh, 2004). Belayneh and Cosgrove (2004) created the 2D fracture pattern using a window sampling approach. First, the limestone outcrop was marked with a grid having a spacing of about 1 m. Then, a number of photographs were taken at a fixed height above the ground and rectified for perspective distortions before assembly. Finally, individual fractures were manually traced from the constructed digital map.

The thin-bed limestone (0.01 m thick) is sandwiched between impervious shales, and dissected by two sets of stratabound, vertically dipping fractures. The E-W striking set that formed in an early stage contains laterally persistent fractures, which tend to arrest the later developed N-S striking set consisting of short fractures. This natural fracture network exhibiting a hierarchical, ladder pattern has been used as an analogue to the subsurface system for studying single-phase flow, multiphase flow, solute transport and thermal conductivity (Edery et al., 2016; Geiger, Cortis, & Birkholzer, 2010; Geiger & Emmanuel, 2010; Lei, Wang, Xiang, & Latham, 2017; Matthäi & Belayneh, 2004; Matthäi, Nick, Pain, & Neuweiler, 2010). In this paper, we represent the system with a two-dimensional (2-D) DFN (Geiger et al., 2010), and use this fracture network to explore the impact of geological stress on single-phase flow and transport behavior.

The material properties of the fractured limestone are assumed to be as follows (N. Barton et al., 1985; Lama & Vutukuri, 1978): the bulk density is 2700 kg/m³, the Young's modulus is 30.0 GPa, the Poisson's ratio is 0.27, the internal friction coefficient is 0.6, the tensile strength is 4.0 MPa, the cohesive strength is 8.0 MPa, the mode I and II energy release rates are 20.0 and 100.0 J/m², respectively, the residual friction coefficient is 0.6; the properties of rough fractures are based on a laboratory fracture sample of length $l_0 = 0.2$ m, such that the joint roughness coefficient $JRC_0 = 15$ and the joint compressive strength $JCS_0 = 120$ MPa.

We assume that the initial apertures a_0 (under no stress loading) follow a lognormal distribution with a mean value of 1 mm and a variance of 0 (i.e. constant aperture scenario) or

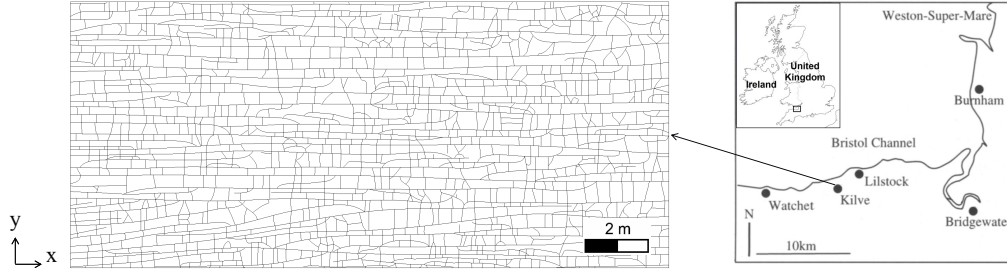


Figure 1. An 18 m by 8 m fracture network mapped at the limestone exposure at the south margin of the Bristol Channel Basin, UK (Belayneh, 2004).

1 (i.e. variable aperture scenario). We randomly assign the lognormally-distributed aperture values to different fracture sections (or links) that connect adjacent intersection nodes, such that each link has an assigned initial aperture value but different links may have different values in the variable aperture case. The use of lognormal distribution is supported by many previous field observations and modeling studies (Bonnet et al., 2001; Cacas, Ledoux, Marsily, et al., 1990; de Dreuzy, Davy, & Bour, 2001; Dverstorp & Andersson, 1989; Long & Billaux, 1987; Neuman & Di Federico, 2003; Pyrak-Nolte, Montemagno, & Nolte, 1997; Snow, 1970). Here, we focus on the aperture variability effect, and do not explore the complex correlation between fracture apertures and other properties such as length and orientation. We impose effective far-field principal stresses orthogonally to the fracture network, and explore a range of different stress scenarios, including the reference case ($S_x = S_y = 0$), two isotropic stress conditions ($S_x = S_y = 5, 15$ MPa), and two anisotropic stress conditions ($S_x = 5$ MPa, $S_y = 15$ MPa, and $S_x = 15$ MPa, $S_y = 5$ MPa). The stress scenarios explored here may represent the condition at a depth around 500 m, which is a typical depth for nuclear waste disposal sites and shallow mineral mining sites.

2.2 Geomechanical model

We simulate the geomechanical behavior of fractured rocks using the finite-discrete element method (FDEM) (Munjiza, 2004), which can capture the deformation of intact rocks, displacement of pre-existing fractures and propagation of new cracks (Lei, Latham, & Tsang, 2017; Lei et al., 2014). We explicitly resolve each fracture as a discrete entity, which permits analyzing the impact of geological stress and fracture geometrical properties on fluid flow and transport. The FDEM model represents a 2-D fractured rock using a fully discontinuous mesh

of three-node triangular finite elements linked by four-node broken (representing discontinuities) or unbroken (representing rock matrix) joint elements (Lei, Latham, & Xiang, 2016). The motions of linear-elastic, constant-strain finite elements are governed by Newton's second law:

$$\mathbf{M}\ddot{x} + \mathbf{F}_{\text{int}} = \mathbf{F}_{\text{ext}} = \mathbf{F}_l + \mathbf{F}_b + \mathbf{F}_c, \quad (1)$$

where \mathbf{M} is the lumped nodal mass matrix, x is the vector of nodal displacements, \mathbf{F}_{int} are the internal nodal forces induced by the deformation of finite elements, \mathbf{F}_{ext} are the external nodal forces consisting of external loads \mathbf{F}_l contributed by boundary and body forces, cohesive bonding forces \mathbf{F}_b caused by the deformation of unbroken joint elements, and contact forces \mathbf{F}_c generated by the contact interaction via broken joint elements.

To capture the nonlinear deformation of natural rough fractures under normal and/or shear loadings, an empirical joint constitutive model has been implemented into the FDEM framework (Lei et al., 2016). The compression-induced fracture closure is characterized by a hyperbolic relation (Bandis et al., 1983):

$$\eta_n = \frac{\sigma_n \eta_m}{k_{n0} \eta_m + \sigma_n}, \quad (2)$$

where η_n is the current compression-induced closure (mm), σ_n is the effective normal stress (MPa), k_{n0} is the initial normal stiffness (MPa/mm), and η_m is the maximum allowable closure (mm). The values of k_{n0} and η_m are estimated using (Bandis et al., 1983):

$$k_{n0} = -7.15 + 1.75\text{JRC} + 0.02 \times \frac{\text{JCS}}{a_0}, \quad (3)$$

$$\eta_m = -0.1032 - 0.0074\text{JRC} + 1.1350 \times \left(\frac{\text{JCS}}{a_0} \right)^{-0.2510}, \quad (4)$$

where a_0 is the initial aperture (mm), JRC is the joint roughness coefficient and JCS is the joint compressive strength (MPa). Both JRC and JCS are scale-dependent (Bandis, Lumsden, & Barton, 1981) and their field-scale values, i.e. JRC_n and JCS_n , are estimated using the scaling laws (N. Barton et al., 1985):

$$\text{JRC}_n = \text{JRC}_0 \left(\frac{l_{ij}}{l_0} \right)^{-0.02\text{JRC}_0}, \quad (5)$$

$$\text{JCS}_n = \text{JCS}_0 \left(\frac{l_{ij}}{l_0} \right)^{-0.03\text{JCS}_0}, \quad (6)$$

where l_{ij} is the field-scale effective fracture length (i.e. size of the link connecting adjacent intersection nodes i and j), JRC_0 and JCS_0 are based on the laboratory sample of length l_0 .

A rough fracture under shear displacement tends to dilate and the increment of dilational displacement is given by (Olsson & Barton, 2001):

$$d\eta_s = -\tan \phi_{\text{mob}} d\varepsilon, \quad (7)$$

where $d\eta_s$ is the increment of normal displacement caused by shear dilation, $d\varepsilon$ is the increment of shear displacement, and ϕ_{mob} is the mobilized dilation angle given by (Olsson & Barton, 2001):

$$\phi_{\text{mob}} = \frac{1}{\zeta} \text{JRC}_{\text{mob}} \log_{10} \left(\frac{\text{JCS}_n}{\sigma_n} \right), \quad (8)$$

with the damage coefficient ζ given by (N. Barton & Choubey, 1977):

$$\zeta = \frac{\text{JRC}_n}{12 \log_{10} \left(\frac{\text{JCS}_n}{\sigma_n} \right)} + 0.70, \quad (9)$$

The mobilized joint roughness coefficient JRC_{mob} is related to the ratio of the current shear displacement ε to the peak shear displacement ε_p (N. Barton et al., 1985), which is given by:

$$\varepsilon_p = \frac{l_{ij}}{500} \left(\frac{\text{JRC}_n}{l_{ij}} \right)^{0.33}, \quad (10)$$

The increment of total normal displacement under combined normal and shear loadings is thus derived as:

$$d\eta = d\eta_n + d\eta_s, \quad (11)$$

such that the mechanical aperture a is further calculated as (Lei et al., 2016):

$$a = \begin{cases} a_0 + o, & o \geq 0, \\ a_0 - \eta, & o < 0, \end{cases} \quad (12)$$

where o is the separation of the opposite walls when the fracture is under extension, and η is the accumulative closure when the fracture is under compression. The hydraulic aperture, i.e. the equivalent aperture for laminar flow through fractures, is assumed equal to the mechanical aperture (Baghbanan & Jing, 2008; Matthäi & Belayneh, 2004; Min et al., 2004; Nick et al., 2011; Paluszny & Matthai, 2010).

2.3 Flow and transport model

2.3.1 Flow

We model laminar, incompressible fluid flow through the fracture network, and use the cubic law (Witherspoon et al., 1980) to describe fluid flow in each individual fracture. We consider flow through fractures only, and disregard fracture-matrix interactions, in order to focus on geomechanical effects on flow and transport through the fracture network. The flow rate between nodes i and j is given by:

$$Q_{ij} = W \frac{\rho g a_{ij}^3}{12\mu} \frac{h_j - h_i}{l_{ij}}, \quad (13)$$

where W is the thickness of the limestone bed, l_{ij} the length and a_{ij} the hydraulic aperture of the fracture connecting nodes i and j , h_i is the hydraulic head at node i , ρ is the water density, g is gravitational acceleration, μ is the water viscosity. We impose mass conservation constraint at each node i , $\sum_j Q_{ij} = 0$. The hydraulic head values at every node can be obtained by solving the mass conservation equation with the cubic law (13), which gives a linear system of equations. The average fluid flow velocity through each fracture link is obtained by dividing the flow rate by the fracture cross-sectional area,

$$u_{ij} = \frac{Q_{ij}}{W a_{ij}}. \quad (14)$$

We study a uniform flow setting by imposing constant hydraulic head values at the left and right boundaries and imposing no-flow conditions at the top and bottom boundaries of the fracture network. This gives a mean flow direction from left to right across the domain. The heterogeneity of the flow field can be quantified with the probability density function (PDF) of the Eulerian velocity, which can be obtained by sampling velocity values at every link weighted by the link length,

$$p_e(u) = \frac{\sum_{i>j} l_{ij} \delta(u - |u_{ij}|)}{\sum_{i>j} l_{ij}}, \quad (15)$$

where N_l is the number of links, δ is the Dirac delta function, and the overbar $\overline{(\cdot)}$ denotes the average over all realizations of a given scenario.

2.3.2 Transport

We model passive solute transport with particle tracking simulations. Once we obtain the velocity fields, we run particle tracking simulations to derive transport statistics. We simulate advective transport of a passive tracer where each tracer particle moves with the average velocity at each link. We inject particles at the left (inlet) boundary with flux-weighted probability, which means that the number of particles injected at each inlet node is proportional to the flow rate at that inlet node. We inject 10^5 particles for constant initial aperture cases, and 10^4 particles into each realization for the heterogeneous initial aperture cases. We consider 20 realizations for each heterogeneous scenario.

At fracture intersections, we apply a complete mixing rule, which is the most commonly used particle routing rule at intersections (Berkowitz & Scher, 1997; Kang, Dentz, Le Borgne, & Juanes, 2015; Park et al., 2001; Willmann, Lanyon, Marschall, & Kinzelbach, 2013). The complete mixing rule assumes that fluids are well mixed at intersections and the probability of a particle exiting through an outgoing link is proportional to the flow rate through that link. The complete mixing rule implies that local Péclet number at each intersection is small enough that diffusion can homogenize the concentration field. The choice of the mixing rule can have a major impact on transverse spreading, but was shown to have a negligible effect on longitudinal spreading (Kang, Dentz, et al., 2015; Park et al., 2001; Sherman, Hyman, Bolster, Madeonska, & Srinivasan, 2019). In this study, we limit our analysis to longitudinal spreading and therefore the choice of a particular mixing rule at intersections does not affect our conclusions.

The average solute spreading behavior is quantified with the first passage time distribution which is also known as breakthrough curve (BTC). BTC is the PDF of particle arrival times at a control plane located at certain distance $x = x_c$. We fix the control plane to the outlet (right boundary). The BTC, $f(\tau, x_c)$, is obtained by averaging particle arrival times over particles and realizations,

$$f(\tau, x_c) = \overline{\langle \delta(\tau - t_c) \rangle}, \quad (16)$$

where t_c is the particle arrival time at the control plane x_c . Note that the angular brackets $\langle \cdot \rangle$ denote the average over all particles, and the overbar denotes the ensemble average over all realizations of a given scenario.

3 Results

We present the modeling results of geomechanical deformation, fluid flow and solute transport in the natural fracture networks. We first discuss the cases where the fracture network is associated with a constant initial aperture field (i.e. the variance of initial aperture PDF is 0), and then discuss the cases of a variable initial aperture field (i.e. the variance of initial aperture PDF is 1) for which an ensemble of 20 realizations is used. Note that both cases have an identical initial mean aperture of 1 mm.

3.1 Constant initial aperture case

3.1.1 Geomechanical deformation

The spatial maps of aperture values for the fracture networks under different far-field stress loading conditions are shown in Figure 2. When $S_x = S_y = 0$ MPa, all fractures have aperture values equal to the prescribed initial value of 1 mm (Figure 2a). If the fractured rock is isotropically stressed, the fractures mainly experience normal deformation and the aperture field is fairly homogeneous (Figure 2b-c). As the stress magnitude is increased to 5 MPa, all fractures are closed under the isotropic compression and exhibit apertures significantly smaller than the initial value (Figure 2b). If the stress load is further increased to 15 MPa, fractures tend to be more closed but less sensitive to the enhanced compression (note the similar aperture maps between Figure 2b and 3c), due to the nonlinear normal deformation behavior of rough fractures, Equation (2). If the fractured rock is anisotropically stressed, differential stresses will be accommodated in the fractured rock, which may trigger shear deformation along some of the fractures with preferential orientation and good connectivity. For example, if $S_x = 15$ MPa and $S_y = 5$ MPa (Figure 2d), some of the through-going fractures of the E-W set, which exhibit curved traces and are oriented (or partially oriented) obliquely to the direction of the maximum principal stress, i.e. S_x , are significantly sheared and dilated with their apertures being larger than the initial value. However, if $S_x = 5$ MPa and $S_y = 15$ MPa (Figure 2e),

the aperture field is fairly homogeneous, because the E-W fracture set of good connectivity is not preferentially oriented to the direction of the maximum principal stress, i.e. S_y . The N-S set that may be preferentially oriented to the direction of the maximum principal stress is also prevented from sliding due to the constraint of the rock matrix.

We compare the distributions of fracture apertures under different loading conditions based on aperture PDFs (Figure 3). Without any stress loading, the fracture network is associated with a constant aperture value of 1 mm (Figure 3). With an increase of the isotropic stress magnitude, the mean value of fracture apertures decreases, and there is some spread in the aperture distribution due to the scale-dependence of fracture properties (i.e. JRC_n and JCS_n in Equations (5)-(6)) such that different links with distinct lengths exhibit slightly different closure behaviors. It can also be seen that the fracture closure is more sensitive to stress when the stress magnitude is low, as predicted by the hyperbolic relation between normal stress and fracture closure, Equation (2). Note that the PDFs of different non-zero isotropic stresses exhibit a similar Gaussian-like distribution. However, if the fractured rock is anisotropically stressed, the two cases exhibit very different shapes for the aperture PDF (Figure 3b). When $S_x = 5$ MPa and $S_y = 15$ MPa, the PDF has a small spread around its mean value, which is smaller than the initial value of 1 mm due to the closure of fractures. Further, the N-S and E-W fracture sets tend to have similar aperture values due to their little sensitivity to stress under high stress loading, such that the PDF has a unimodal form. In contrast, when $S_x = 15$ MPa and $S_y = 5$ MPa, the aperture PDF exhibits two regimes: a Gaussian-like distribution regime for small aperture values due to the compression-induced fracture closure, and a broad distribution regime at larger aperture values due to shear dilation-induced large apertures. This broad regime follows an exponential distribution with a rate parameter of about 5 and exhibits aperture values significantly larger than their initial value of 1 mm.

3.1.2 Flow field

We obtain the flow rate distribution by solving the linear system of equations obtained by combining the mass conservation constraint with the cubic law (Equation (13)). The flow velocity is then obtained according to Equation (14). To facilitate the comparison, we normalize velocity values with the mean velocity value of the zero stress loading case (i.e. $S_x = S_y = 0$ MPa). As shown in Figure 4, the E-W horizontal fracture set shows significantly higher flow velocity compared to the N-S vertical set. This is because the horizontal fracture set is aligned with the mean flow direction. With the increase of isotropic stress magnitude (Figure 4b-c),

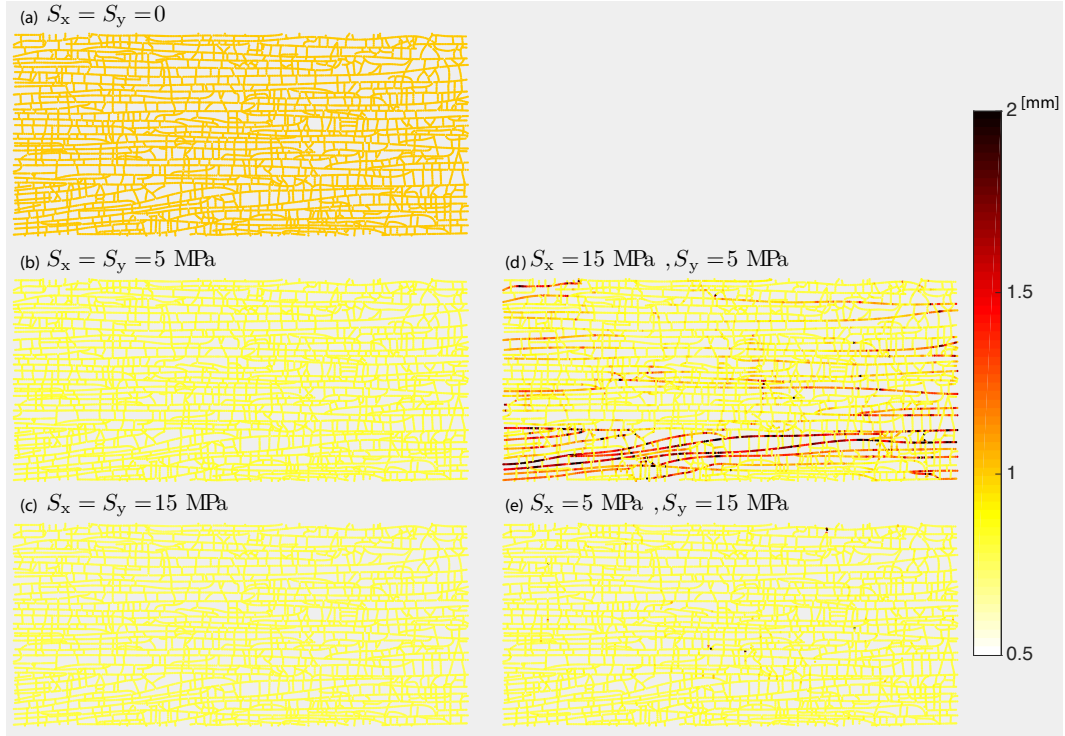


Figure 2. Spatial maps of aperture values at various geomechanical stress conditions for constant initial aperture cases. (a) When $S_x = S_y = 0$ MPa, all fractures have aperture values identical to the prescribed initial value of 1 mm. (b) Isotropic stress condition with the stress magnitude 5 MPa. (c) Isotropic stress condition with the stress magnitude 15 MPa. (d) Anisotropic stress condition with $S_x = 15$ MPa and $S_y = 5$ MPa. (e) Anisotropic stress condition with $S_x = 5$ MPa and $S_y = 15$ MPa.

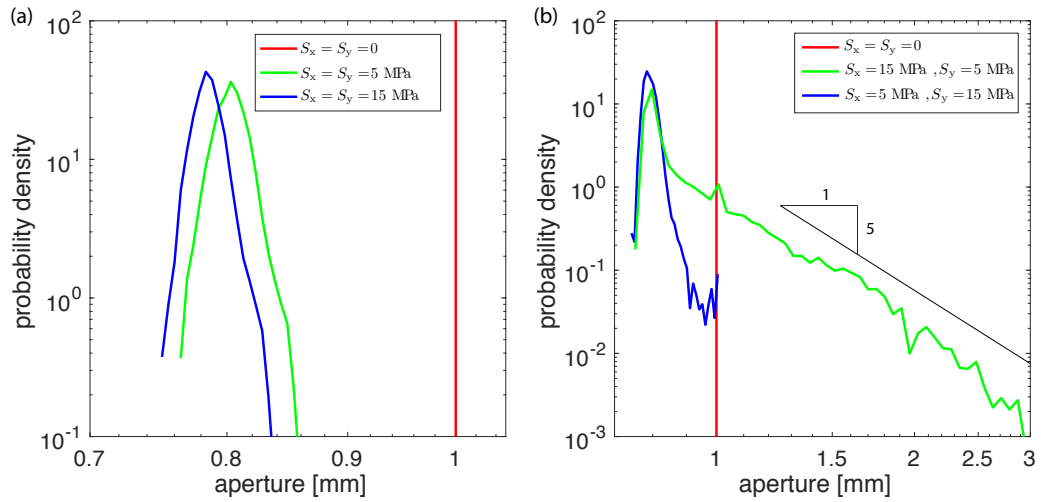


Figure 3. Aperture PDFs for constant initial aperture cases. (a) The isotropic stress conditions. (b) The anisotropic stress conditions.

the flow velocity is significantly reduced due to the compression-induced normal closure of fractures. For the anisotropic far-field stress loading, the flow field is very heterogeneous when $S_x = 15$ MPa and $S_y = 5$ MPa due to the pronounced shear dilation along some of the fractures (Figure 4d), but still fairly homogeneous when $S_x = 5$ MPa and $S_y = 15$ MPa (Figure 4e) due to the lack of shear dilation.

We further analyze the impact of geological stress on velocity fields with the Eulerian velocity PDFs, Equation (15). As shown in Figure 5a, the PDF for the case of no stress loading exhibits a clear bimodal shape. The left peak corresponds to the regime of low flow velocities through the N-S set of short fractures, whereas the second peak represents the regime of high flow velocities accommodated by the E-W set of through-going fractures (aligned with the mean flow direction). If the fractured rock is isotropically stressed, the bimodal PDF shape is maintained but the velocity magnitude decreases as the stress level increases (Figure 5a). Due to the nonlinear normal deformation behavior of rough fractures, the difference between the isotropic 5 MPa case and the isotropic 15 MPa case is small (fracture deformation becomes insensitive to stress variation when the stress level is high enough). If the fractured rock is anisotropically stressed, the case of $S_x = 5$ MPa, $S_y = 15$ MPa shows similar behavior as those under isotropic stress loadings, but the case of $S_x = 15$ MPa, $S_y = 5$ MPa shows a significantly broadened velocity PDF. The dual modal form remains but the velocity magnitude can be much larger than that under no stress loading (Figure 5b inset). This is a noteworthy observation that indicates the interplay between fracture network geometry and stress condition can lead to anomalously fast flow paths.

3.1.3 Transport behavior

We run particle tracking simulations to obtain transport properties. The focus in this study is the longitudinal spreading and we quantify it with BTCs, Equation 16. For isotropic stress conditions, the stress-induced fracture closure simply delays the arrival times of particles and has a minor impact on longitudinal spreading (Figure 6(a)). For the anisotropic stress condition with $S_x = 15$ MPa and $S_y = 5$ MPa, we observe an anomalously early arrival of tracers and the longitudinal spreading is considerably enlarged (Figure 6b), as a result of shear dilation-induced preferential flow paths. However, if $S_x = 5$ MPa and $S_y = 15$ MPa, the fracture deformation is governed by normal closure and thus the effect of stress loading mainly causes retarded particle arrivals (Figure 6b), like in the isotropic stress conditions.

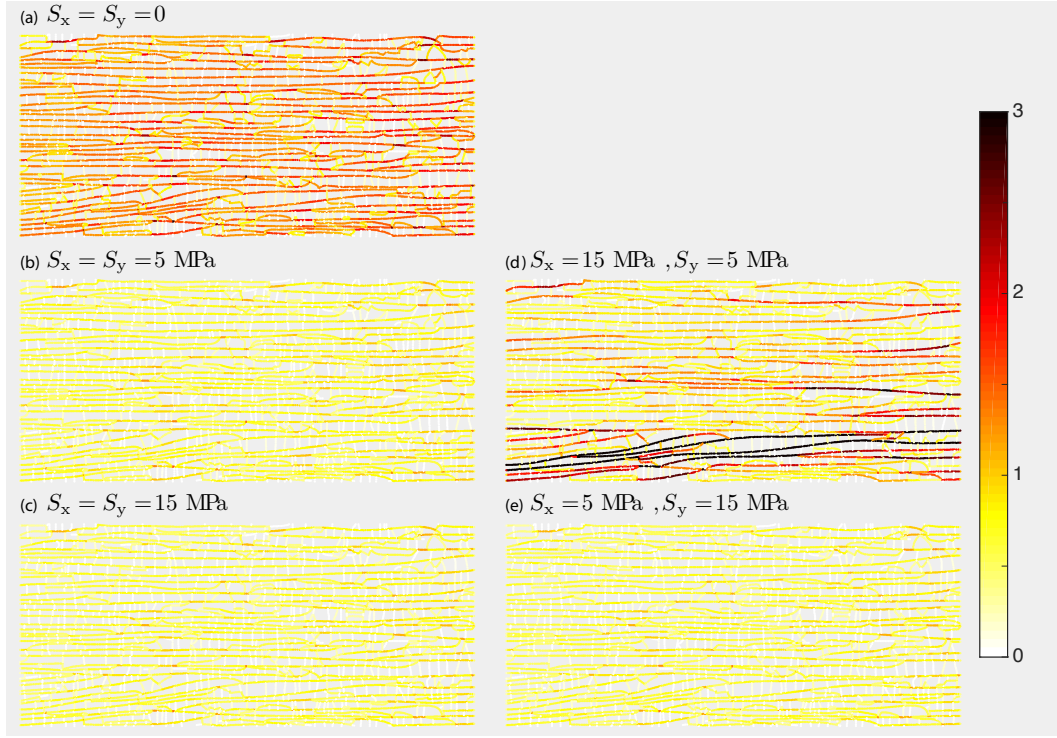


Figure 4. Normalized flow velocity fields for constant initial aperture cases. Velocity values are normalized with the mean velocity of the zero stress loading case (i.e. $S_x = S_y = 0$ MPa).

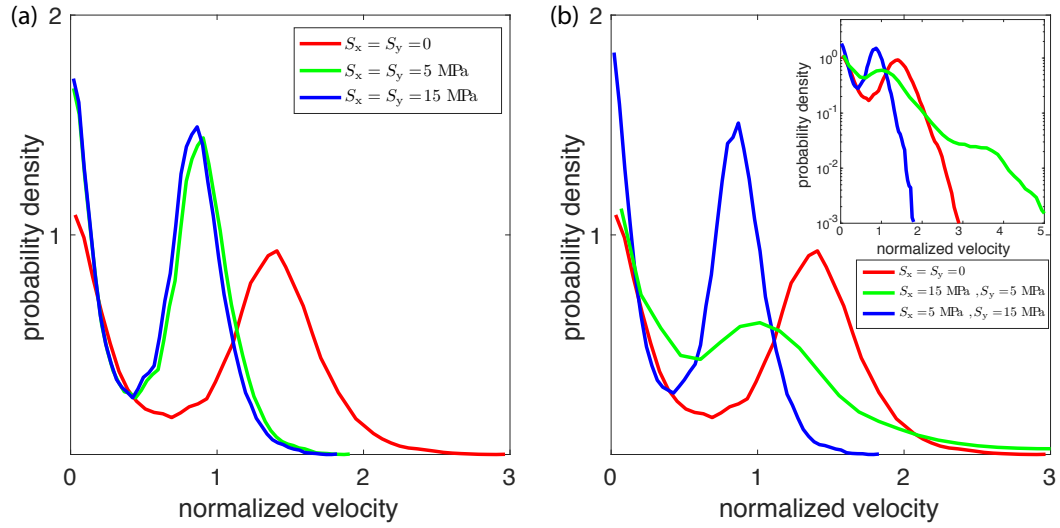


Figure 5. Eulerian velocity PDFs for constant initial aperture cases. (a) Isotropic stress conditions. (b) Anisotropic stress conditions. inset: the semilogy plot showing high velocity values for the anisotropic stress condition with $S_x = 15$ MPa and $S_y = 5$ MPa.

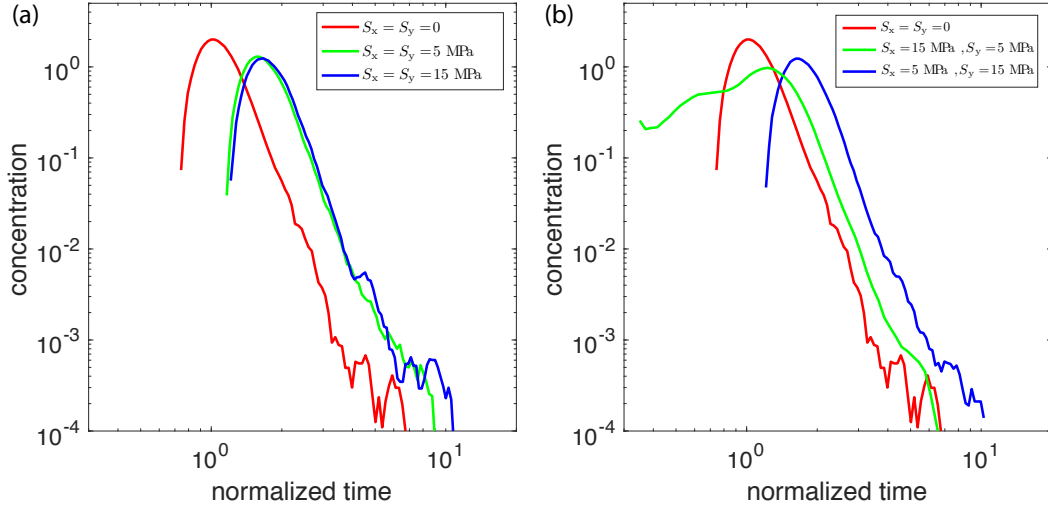


Figure 6. Breakthrough curves at the outlet for constant initial aperture cases. (a) BTCs for isotropic stress conditions. (b) BTCs for anisotropic stress conditions. Tracer arrival times are normalized with the peak arrival time of the zero stress loading case.

3.2 Variable initial aperture case

3.2.1 Geomechanical deformation

The spatial maps of aperture values for the variable initial aperture case under different far-field stress conditions are shown in Figure 7. Note that the initial aperture distribution follows a lognormal distribution with a mean value of 1 mm and a variance of 1. The initial aperture map shows highly variable aperture values (Figure 7a), such that the stress-induced aperture variation is not easy to discern. A qualitative visual comparison suggests an overall decrease of apertures as the stress magnitude increases in most stress conditions (Figure 7b,c,e), but aperture increase seems to occur along some E-W oriented fractures in the case of $S_x = 15$ MPa and $S_y = 5$ MPa (Figure 7d). The effect the aperture increase on flow and transport is analyzed in Sections 3.2.2 and 3.2.3.

The stress effect on aperture distribution is evident from the PDFs of fracture apertures (Figure 8). For isotropic stress conditions, aperture values decrease as the stress magnitude increases (Figure 8a) due to the compression-induced fracture closure, similar to those in the constant initial aperture case (Figure 3a). However, the width of the distribution of log-apertures increases considerably as the stress level increases (Figure 8a, inset), which is different from that of the constant initial aperture case. This is because fractures with large initial apertures

are more compliant than those with small initial apertures, as revealed by Equations (3)-(4). Thus, the aperture PDFs under loading conditions broaden towards small velocities as a result of the significant closure of initially large apertures (with low stiffness) and slight closure of initially small apertures (with high stiffness).

For the anisotropic stress conditions, apertures also reduce due to the dominant normal closure effect. When $S_x = 15$ MPa and $S_y = 5$ MPa, the compression-induced aperture decrease is compromised by the shear dilation-induced aperture increase (Figure 8b). However, the accumulation of small aperture values is evident in both anisotropic cases (Figure 8b, inset). To further elucidate this phenomenon, we remove all the fractures with apertures larger than 0.1 mm and only show those with apertures less than 0.1 mm in Figure 9. As the stress level increases, more apertures smaller than 0.1 mm clearly appear due to the closure of fractures with initial apertures larger than 0.1 mm. On the other hand, the fractures with very small initial apertures, e.g. close to 0.01 mm, are more resistant to normal compression with less closure accommodated. Note that the small aperture values are randomly distributed and do not show correlated spatial organization.

3.2.2 Flow

The normalized fluid flow velocity fields through the fracture network under different far-field stress conditions are shown in Figure 10. We normalize the velocity values using the mean velocity in the case of zero stress loading (i.e. $S_x = S_y = 0$ MPa). A heterogeneous flow pattern characterized by significant flow localizations emerges in the network under no stress loading (Figure 10a) due to the prescribed initial aperture variability. When the fracture deformation is dominated by normal closure (Figure 10b,c,e), the velocity magnitude is greatly reduced due to the increased compressive stress. However, if shear deformation is dominant, as is the case when $S_x = 15$ MPa and $S_y = 5$ (Figure 10d), anomalously large flow velocities occur in some of the W-E fractures that are considerably sheared and dilated.

The impact of stress loading on the flow field is further analyzed based on the Eulerian velocity PDF (Equation 15). As shown in Figure 11, the Eulerian velocity PDF follows a truncated power-law distribution with an exponential cut-off in the large velocity regime. Due to the large initial aperture heterogeneity, no bimodal distribution is found (in contrast with the case of constant initial aperture case, Figure 5). For isotropic stress conditions, the probability of small velocities increases as the stress level increases, and the power-law scaling of the

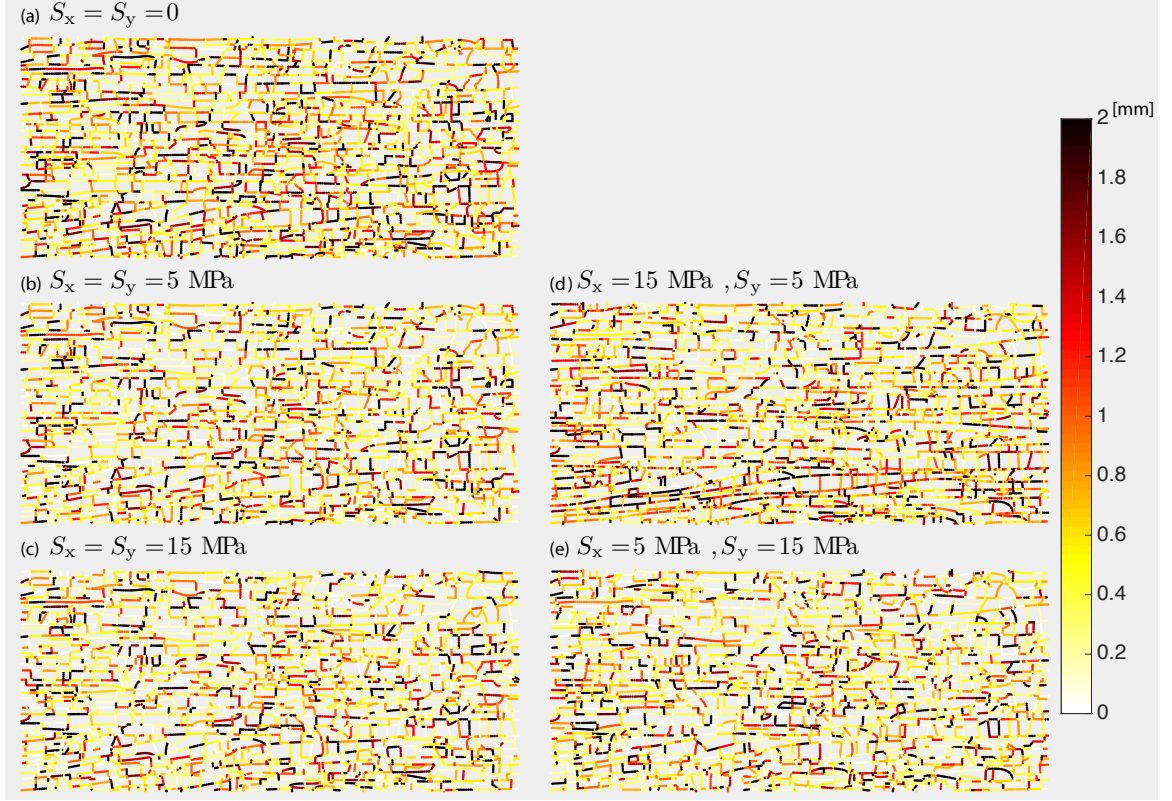


Figure 7. Spatial maps of aperture values at various geomechanical stress conditions for variable initial aperture cases. (a) Initial aperture field at $S_x = S_y = 0$ MPa shows strong aperture heterogeneity. (b) Isotropic stress condition with the stress magnitude 5 MPa. (c) Isotropic stress condition with the stress magnitude 15 MPa. (d) Anisotropic stress condition with $S_x = 15$ MPa and $S_y = 5$ MPa. (e) Anisotropic stress condition with $S_x = 5$ MPa and $S_y = 15$ MPa.

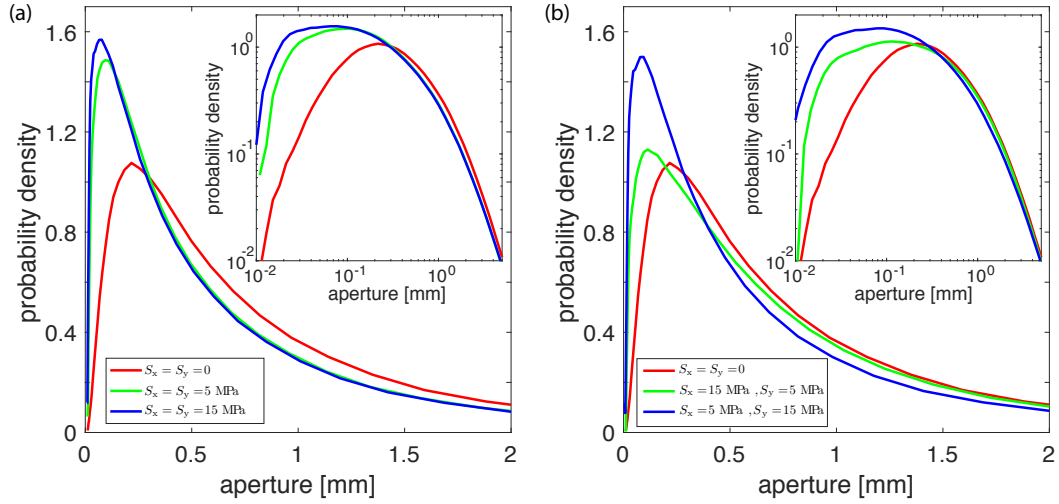


Figure 8. Aperture PDFs for variable initial aperture cases. (a) Isotropic stress conditions. inset: log-log plot. (b) Anisotropic stress conditions. inset: log-log plot.

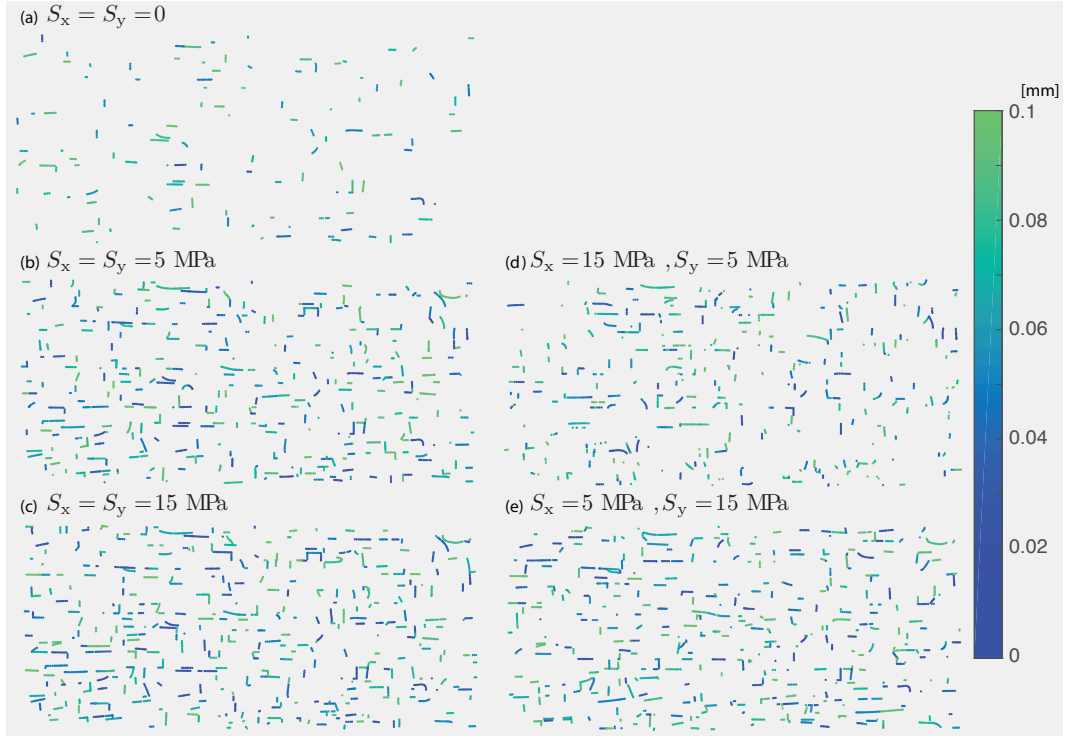


Figure 9. Spatial maps of aperture values that are smaller than 0.1 [mm]. (a) Initial aperture field at $S_x = S_y = 0$ MPa. (b) Isotropic stress condition with the stress magnitude 5 MPa. (c) Isotropic stress condition with the stress magnitude 15 MPa. (d) Anisotropic stress condition with $S_x = 15$ MPa and $S_y = 5$ MPa. (e) Anisotropic stress condition with $S_x = 5$ MPa and $S_y = 15$ MPa.

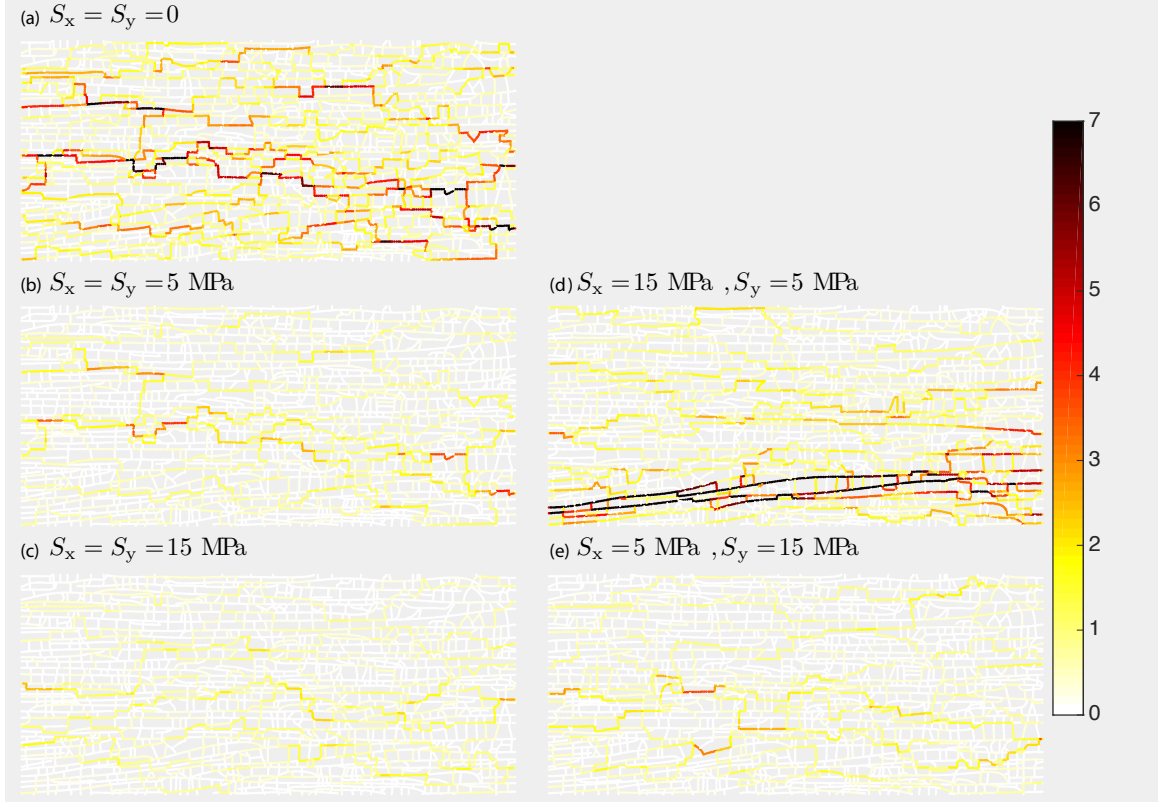


Figure 10. Normalized flow velocity fields for variable initial aperture cases. Velocity values are normalized with the mean velocity of the variable initial aperture case under the zero stress loading (i.e. $S_x = S_y = 0$ MPa).

small velocity values is sensitive to the stress loading (Figure 11a). The fracture network under anisotropic stress conditions also shows an increased fraction of small velocities. Furthermore, large velocity values in the case of $S_x = 15$ MPa, $S_y = 5$ are larger than those in the no stress condition (Figure 11b, inset) due to the shear dilation-induced aperture increase along some of the E-W fractures. The velocity PDFs show that the interplay between fracture network geometry and stress conditions can significantly impact both fast and slow velocities.

3.2.3 Transport

We study the effective transport properties of the stressed fracture network based on the longitudinal spreading, quantified by the BTC analysis. For isotropic stress conditions (Figure 12a), an increased stress magnitude not only delays the arrival time of particles due to the compression-induced reduction of apertures, but also promotes the late-time tailing phenomenon

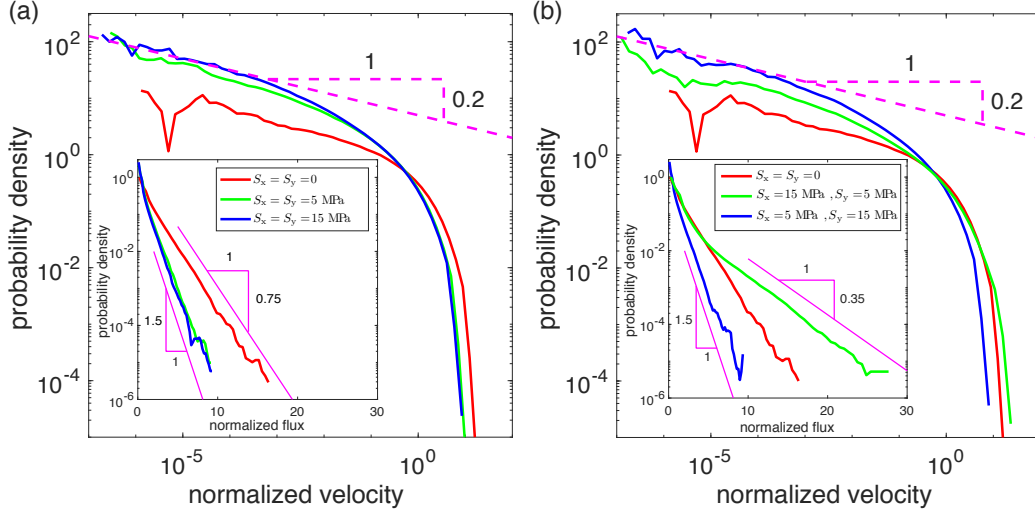


Figure 11. Eulerian velocity PDFs for variable initial aperture cases. (a) Isotropic stress conditions. inset: semilog plot. (b) Anisotropic stress conditions. inset: semilog plot showing the shear dilation-induced high velocity values for $S_x = 15$ MPa and $S_y = 5$ MPa case.

caused by the accumulation of small apertures. For anisotropic stress conditions, if $S_x = 5$ MPa and $S_y = 15$ MPa, a similar stress-dependent transport behavior is observed. However, if $S_x = 15$ MPa and $S_y = 5$ MPa, we observe an anomalously early arrival of tracers and the longitudinal spreading significantly increases due to the strong preferential flow channels produced by the shear dilation effect (Figure 12b).

We consider that the accumulation of small apertures in the stressed fracture network results in the emergence of small velocities and the late-time tailing behavior, while the shear dilation-induced large apertures along some through-going fractures lead to spatially correlated preferential flow paths and the anomalously early arrival feature. The origin of anomalous transport can also be understood as the interplay between velocity distribution and velocity correlation (Kang, Le Borgne, et al., 2015; Le Borgne, Dentz, & Carrera, 2008). The late-time tailing is caused by the broadening of velocity distribution towards small velocity values. The fractures providing small velocities for fluid flow act as trapping zones, which tend to delay the migration of particles. On the other hand, the anomalously early arrival is caused by the spatially correlated large velocity values along the E-W fractures that connect the inlet to the outlet with large openings. Tracers that are transported through these preferential flow paths maintain velocity correlation that leads to early arrivals. To confirm the underlying mechanisms of

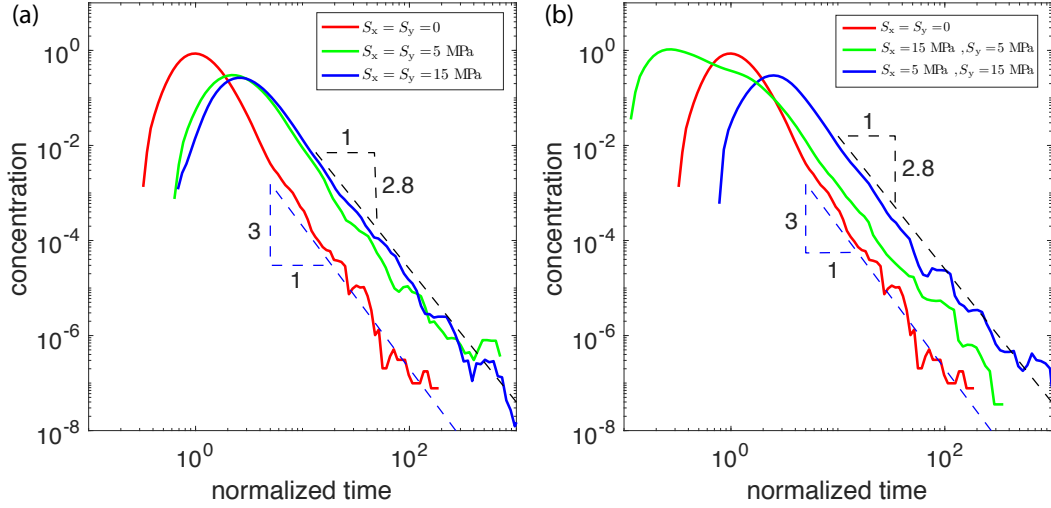


Figure 12. Breakthrough curves at the outlet for variable initial aperture cases. (a) BTCs for isotropic stress conditions. (b) BTCs for anisotropic stress conditions. Tracer arrival times are normalized with the peak arrival time of the zero stress loading case.

the observed transport behaviors, we construct an effective average transport model (Dentz, Kang, Comolli, Le Borgne, & Lester, 2016; Kang et al., 2017) in the following section.

4 Effective stochastic transport model

In this section, we first analyze particle velocities along their trajectories (Lagrangian velocity statistics), and then construct a parsimonious stochastic transport model that effectively captures the interplay between Lagrangian velocity distribution and velocity correlation.

4.1 Space-Lagrangian velocity statistics

We determine the space-Lagrangian velocity PDF $\psi_s(v)$ by sampling particle velocities equidistantly with a lag of $\Delta s = 0.5$ m along all particle trajectories and among all realizations (Dentz et al., 2016; Kang et al., 2017). The chosen lag distance Δs is sufficiently smaller than the characteristic velocity correlation length scale λ_c (see section 4.1.2 for details). From now on, we refer to $\psi_s(v)$ as the velocity distribution.

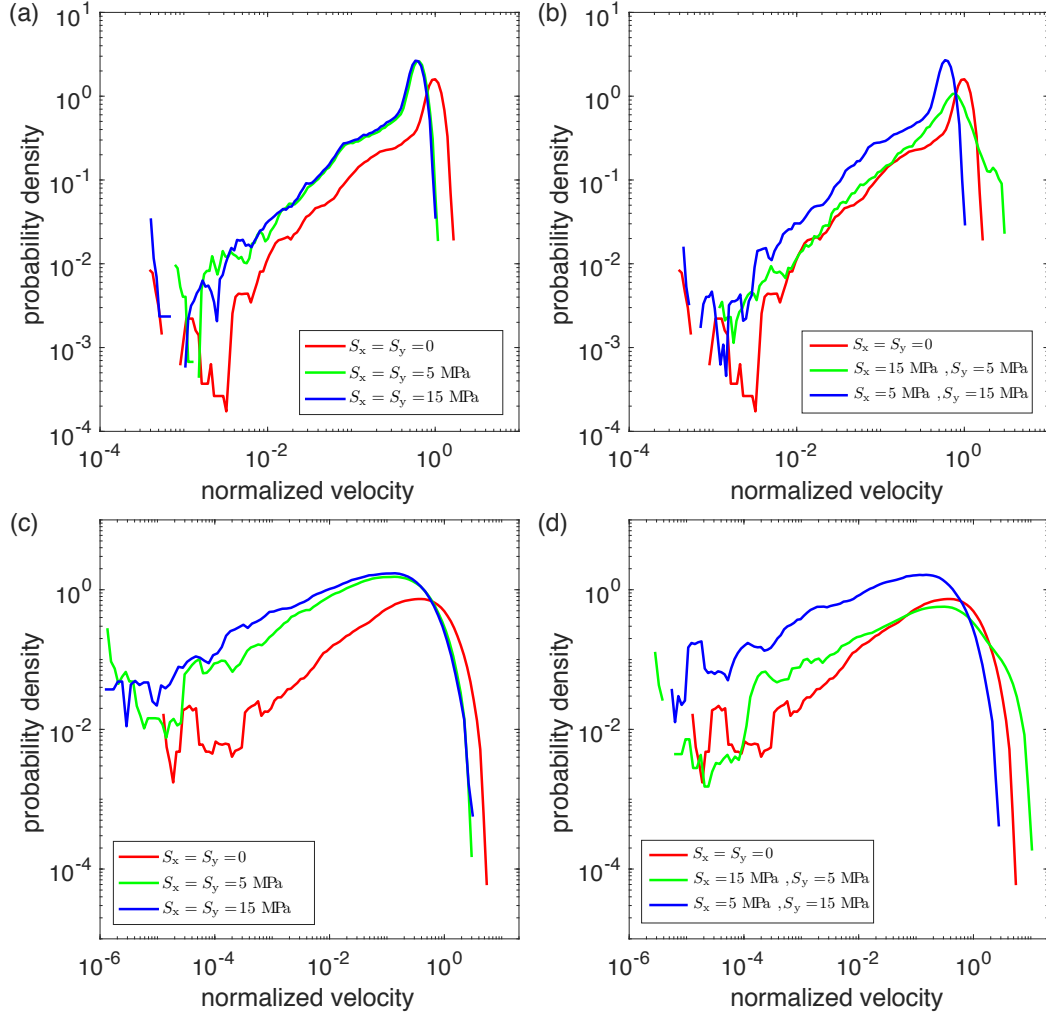


Figure 13. Lagrangian velocity distributions, $\psi_s(v)$. (a) $\psi_s(v)$ for the isotropic stress conditions with constant initial aperture. (b) $\psi_s(v)$ for the anisotropic stress conditions with constant initial aperture. (c) $\psi_s(v)$ for the isotropic stress conditions with variable initial aperture. (d) $\psi_s(v)$ for the anisotropic stress conditions with variable initial aperture.

4.1.1 Velocity distributions

For the constant initial aperture cases, the increase in the isotropic stress magnitude causes a simple translation of the velocity distribution towards lower velocities (Figure 13(a)). Increase in the isotropic stress magnitude does not change the shape or variance of the velocity distributions. For anisotropic stress conditions, when the through-going fractures of the E-W set are sheared ($S_x = 15$ MPa and $S_y = 5$ MPa), we observe the emergence of fast velocities (Figure 13(b)). For $S_x = 5$ MPa and $S_y = 15$ MPa case, the effects of stress on the velocity distribution is similar to the isotropic stress conditions.

The impact of geological stress on velocity distribution is much more dramatic for the variable initial aperture cases. The increase in the isotropic stress magnitude broadens the velocity distribution, and has a significant impact on the scaling of small velocities (Figure 13(c)). For anisotropic stress conditions, when the principal fracture orientation is aligned with the maximum stress orientation ($S_x = 15$ MPa and $S_y = 5$ MPa), we observe both the emergence of fast velocities and significant change in the scaling of the small velocities (Figure 13(d)). The shear-dilation induced preferential channels causes the emergence of fast velocities. For $S_x = 5$ MPa and $S_y = 15$ MPa case, the impact of stress on velocity distribution is similar to the isotropic stress conditions. The major difference between the constant initial aperture cases and the variable initial aperture cases is in the low-velocity values. For the cases with initial aperture heterogeneity, the increase in the stress magnitude significantly broadens the velocity distribution towards small velocities and changes the scaling of small velocities. This is due to the nonlinear normal deformation behavior of rough fractures, as discussed in section 3.2.1.

4.1.2 Velocity correlation lengths

We now analyze the spatial velocity correlation along particle trajectories, which may be sensitive to the initial velocity (Le Borgne et al., 2008). The velocity correlation length conditioned on the initial velocity is determined through the convergence of the conditional Lagrangian velocity PDF $\psi(v, s|v_0)$ towards a steady-state distribution (Le Borgne, de Dreuzy, Davy, & Bour, 2007). If the velocity field is ergodic, $\psi_s(v, \infty|v_0) = \psi_s(v)$ as defined above. The conditional distribution $\psi_s(v, s|v_0)$ is obtained by sampling particle velocities at a distance s from the inlet for all the particles that have an initial velocity in a certain interval $[v_0, v_0 + \Delta v]$. In order to quantify the convergence, we follow Le Borgne et al. (2007) and consider

the distribution $p_\alpha(\alpha, s|\alpha_0)$ of the logarithm of velocity $\alpha = \ln(v)$ conditioned on an initial α in $[\alpha_0, \alpha_0 + \Delta\alpha_0]$. The α range is divided into 5 equiprobable velocity classes for the constant initial aperture cases and 10 equiprobable bins for the variable initial aperture cases. The number of velocity classes chosen provides a meaningful resolution with low noise level. We have confirmed that the velocity correlation length is not sensitive to the number of velocity classes. The PDF of log-velocity α is given in terms of $\psi_s(v, s|v_0)$ by

$$p_\alpha(\alpha, s|\alpha_0) = \exp(\alpha)\psi_s[\exp(\alpha), s|\exp(\alpha_0)]. \quad (17)$$

First, we confirm that $p_\alpha(\alpha, s|\alpha_0)$ for $s \gg \lambda_c$ is independent from α_0 and converges toward $p_\alpha(\alpha) = \exp(\alpha)\psi_s[\exp(\alpha)]$. To determine the rate of convergence toward the asymptotic Lagrangian velocity distribution, we calculate the mean absolute difference between $p_\alpha(\alpha, s|\alpha_0)$ and $p_\alpha(\alpha)$

$$C(s|\alpha_0) = \int_{-\infty}^{\infty} |p_\alpha(\alpha, s|\alpha_0) - p_\alpha(\alpha)| d\alpha, \quad (18)$$

The conditional characteristic correlation length is obtained by integrating the correlation function over distance:

$$\ell_c(v_0) = \int_0^{\infty} \frac{C(s|\ln v_0)}{C(0|\ln v_0)} ds, \quad (19)$$

The conditional correlation lengths are shown in Figure 14. The estimated correlation lengths are significantly larger than the average fracture link length of 0.26 m. For isotropic stress conditions with constant initial aperture, the velocity correlation length is not sensitive neither to the stress magnitude nor the initial velocity (Figure 14(a)). A noticeable difference only emerges for the $S_x = 15$ MPa and $S_y = 5$ MPa, where the velocity correlation length is two times larger for the highest velocity bin (Figure 14(b)). The trend is similar for heterogeneous initial aperture cases. We observe a slight increase in correlation length towards large velocity for isotropic stress conditions but the change is not significant (Figure 14(c)). The significant increase in velocity correlation length towards large velocity bins is also observed for the $S_x = 15$ MPa and $S_y = 5$ MPa case (Figure 14(d)).

It is interesting to note that the velocity correlation length is larger for constant initial aperture cases compared with heterogeneous initial aperture cases. The smaller velocity correlation for the heterogeneous initial aperture is due to the emergence of a more heterogeneous velocity field which leads to strong velocity fluctuations than for the constant initial aperture case. This leads to more heterogeneous particle velocity trajectory, which induces a reduction in velocity correlation. A similar trend has been observed in the recent publication by Kang et al. (2016). Also, the effective correlation length is not very sensitive to the stress conditions, except for the $S_x = 15$ MPa and $S_y = 5$ MPa case. This is more evident from Figure 15, where velocity values are normalized with the mean velocity of their respective stress scenario cases. It is clear that the overall velocity correlation structure is similar for different stress conditions except for the $S_x = 15$ MPa and $S_y = 5$ MPa case.

4.1.3 Tortuosity

Due to the heterogeneous velocity field (Figure 10), particle trajectories can be tortuous and the actual travelled distance of a particle (pathline) is in general larger than the linear travel distance (longitudinal distance in this study). The ratio between pathline length and linear distance is quantified by tortuosity, χ , which can be defined as

$$\chi(x_l) = \frac{\langle \lambda(x_l) \rangle}{x_l}, \quad (20)$$

where $\lambda(x_l)$ is the length of a particle travel path when a particle first arrives at a linear (longitudinal) distance x_l . The tortuosity for the different stress conditions is shown in the inset of Figure 14(a). As expected, the tortuosity of the constant initial aperture cases (red line) is significantly smaller than the tortuosity of the heterogeneous initial aperture cases (blue line). The tortuosity in general increases as the stress magnitude increases because the velocity field becomes more heterogeneous due to the significant increase in small aperture values. The tortuosity of $S_x = 15$ MPa and $S_y = 5$ MPa case is significantly smaller than any other stress conditions (Figure 14(a) inset). This can be attributed to the effect of shear dilation that causes straight preferential flow paths (Figure 10(f)).

4.2 Bernoulli Continuous Time Random Walk model

We now construct an effective transport model that captures the interplay between velocity distribution and velocity correlation of the fracture-network system, as exhibited by the

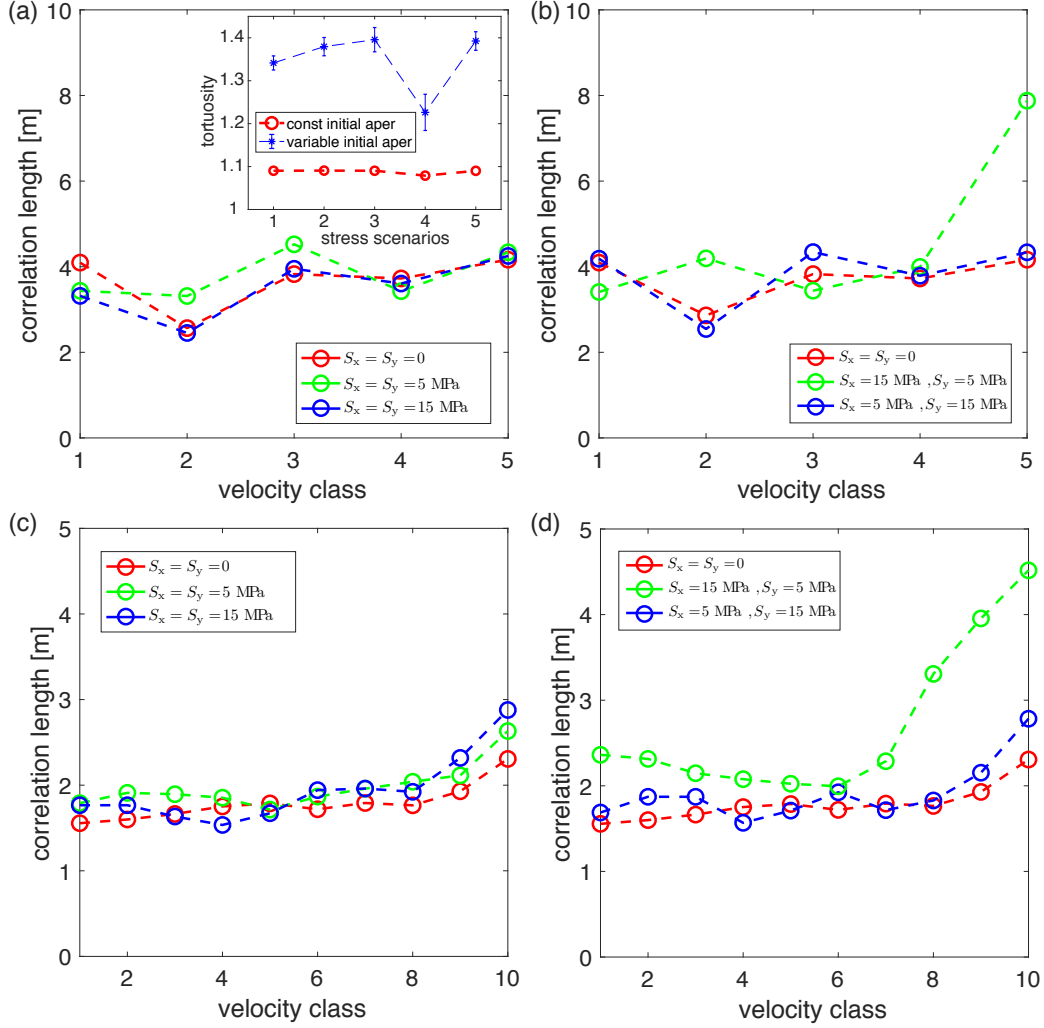


Figure 14. Lagrangian velocity correlation length, $\ell_c(v_0)$, as a function of conditioning initial velocity class. (a) $\ell_c(v_0)$ for isotropic stress conditions with constant initial aperture. Inset: tortuosity for the five stress scenarios ($S_x = S_y = 0$ MPa, $S_x = S_y = 5$ MPa, $S_x = S_y = 15$ MPa, $S_x = 15$ & $S_y = 5$ MPa, $S_x = 5$ & $S_y = 15$ MPa). The length of each blue error bar represents \pm one standard deviation. (b) $\ell_c(v_0)$ for anisotropic stress conditions with constant initial aperture. (c) $\ell_c(v_0)$ for isotropic stress conditions with variable initial aperture. (d) $\ell_c(v_0)$ for anisotropic stress conditions with variable initial aperture.

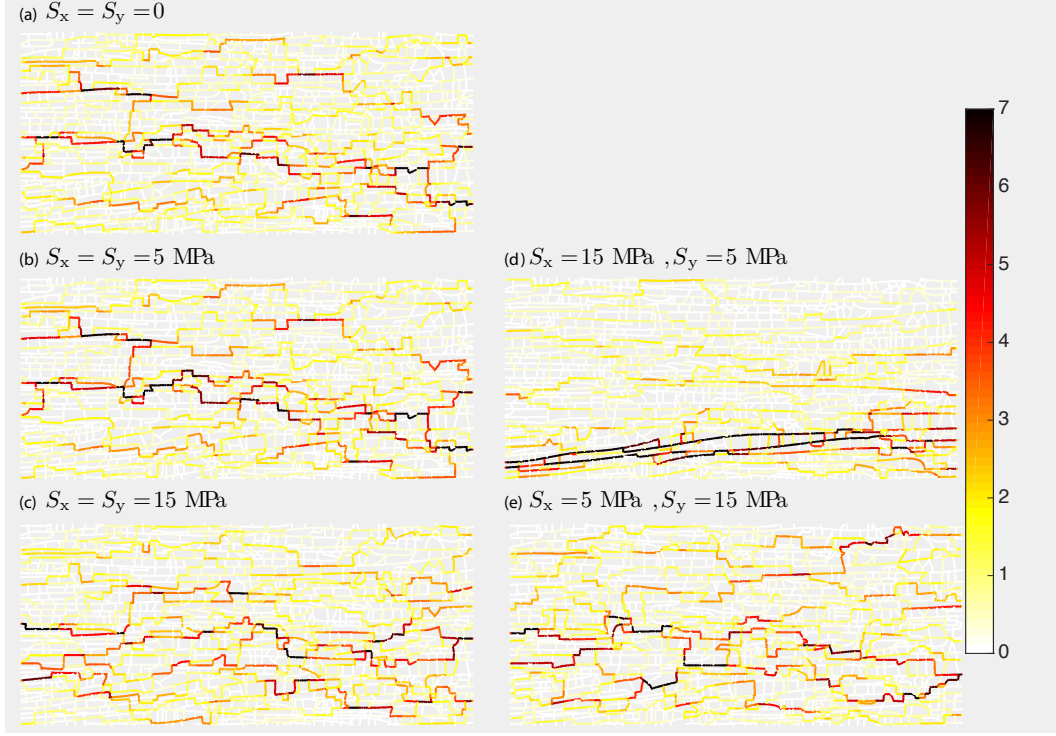


Figure 15. Normalized velocity fields for variable initial aperture cases. Velocity values are normalized with the mean velocity of the respective stress scenario.

direct numerical simulations of particle transport. Recent studies on transport through porous and fracture media at various spatial scales have shown that particle velocities sampled equidistantly in space form a Markov process (Bolster, Méheust, Le Borgne, Bouquain, & Davy, 2014; Kang et al., 2016, 2014, 2017; Le Borgne et al., 2008; Sund, Bolster, & Benson, 2016). We model the velocity series $\{v_n\}$ as a Markov-chain, which is a valid modeling framework for capturing the evolution of the space-Lagrangian velocities when there is a finite velocity correlation length. In this framework, the n -step transition probability $r_n(v|v')$ satisfies the Chapman–Kolmogorov equation (Risken, 1996)

$$r_n(v_n|v_0) = \int dv_k r_{n-k}(v_n|v_k) r_k(v_k|v_0). \quad (21a)$$

The velocity process is fully characterized in terms of the one-step transition PDF $r_1(v|v')$ and the steady state PDF $\psi_s(v)$ of the space-Lagrangian velocity. Consequently, the evolution of the space-Lagrangian velocity PDF $p_s(v, s_n)$ is given by

$$p_s(v, s_n) = \int dv' r_1(v|v') p_s(v', s_{n-1}). \quad (21b)$$

The Markov chain is modeled here by a Bernoulli process, in which the velocity may persist with probability $a = \exp(-\Delta s/\ell_c)$ and change randomly to a velocity drawn from the steady state PDF $\psi_s(v)$. Note that the steady state space-Lagrangian velocity PDF, $\psi_s(v)$, can also be determined by flux-weighting the Eulerian velocity PDF (Dentz et al., 2016), and the model predictions with the space-Lagrangian velocity PDF and the flux-weighted Eulerian velocity PDF should be the same (Kang et al., 2017). The Bernoulli process is characterized by the transition PDF (Dentz et al., 2016; Kang, Le Borgne, et al., 2015)

$$r_1(v|v') = a\delta(v - v') + (1 - a)p_s(v), \quad (22)$$

This transition PDF is thus fully determined by the single parameter ℓ_c , which is estimated by taking average over the conditional correlation length:

$$\ell_c = \frac{1}{N_c} \sum_{i=1}^{N_c} \ell_c(\alpha_i), \quad (23)$$

where N_c is the number of velocity classes and α_i is the logarithmic velocity range of the class i . In this modeling framework, effective particle motion along the trajectory is described by

$$s_{n+1} = s_n + \Delta s, \quad t_{n+1} = t_n + \frac{\Delta s}{v_n}. \quad (24)$$

The velocity transitions are determined from the Markovian velocity process (21). Note that the $\{v_n\}$ process describes equidistant velocity transitions along particle trajectories. To arrive at the control plane at x_l , particles travel the pathline distance of $s(x_l) = \chi(x_l)x_l$ to honor tortuosity of the pathlines. The prediction with the Bernoulli Continuous Time Random Walk (CTRW) model is shown in Figure 16(a)-(d). The model accurately predicts all the BTCs except for the 15 MPa-5 MPa case, for which there is significant preferential flow. We hypothesize that the discrepancy comes from the significantly larger velocity correlation length for large velocity bins (Figure 14). To test this hypothesis, we introduce in the Bernoulli model

two effective velocity correlation lengths, ℓ_h for high velocity classes and ℓ_l for the other velocity classes. Thus, the probability to remain in a high velocity is $a_h = \exp(-\Delta s/\ell_h)$ and $a_l = \exp(-\Delta s/\ell_l)$ for the remaining classes. The transition probability can then be written as

$$r_1(v|v') = a(v')\delta(v - v') + [1 - a(v')]p_s(v), \quad (25)$$

where $a(v') = a_h$ for $v' \geq v_t$ and $a(v') = a_l$ for $v' < v_t$ with v_t the threshold velocity value that defines large velocity classes. More specifically, for the stress condition of 15 MPa-5 MPa, the velocity class 5 defines the high-velocity threshold for the constant initial aperture case, and the velocity classes between 8 and 10 define the high-velocity threshold for the heterogeneous initial aperture case. We take the average correlation lengths for large velocity classes and for the rest of the velocity classes, respectively, to obtain the two correlation lengths. The predictions with the dual correlation length model is shown in Figure 16(e)(f). The dual correlation model better captures both early and late arrivals, showing its ability to properly account for the correlation structure for the cases with significant shear dilation.

5 Discussions and Conclusions

In this study, we have shown how the interplay between fracture properties (aperture distribution and network geometry) and geological stress conditions controls flow and transport in 2D natural fracture networks. We have demonstrated that the geological stress can induce anomalous transport in natural fracture networks. Increase in stress magnitude broadens the aperture PDF towards small apertures, which significantly increases the probability of having small velocity values. Stress-induced broadening of velocity distribution is especially significant when there is initial aperture variability. This is due to the nonlinear normal deformation behavior of rough fractures (Bandis et al., 1983). For anisotropic stress conditions, we show that the orientation between the maximum principal stress and the long fractures is critical. Significant shear dilation occurs when the long fractures are preferentially oriented with respect to the maximum principal stress and accommodate sliding of rough fracture walls (Baghbanan & Jing, 2008; Liu et al., 2018; Olsson & Barton, 2001; Zhao et al., 2011). In summary, the interplay between fracture geometry, aperture heterogeneity and geological stress is shown to induce the emergence of small apertures that causes late-time tailing and the shear dilation that causes anomalously early arrival of particles.

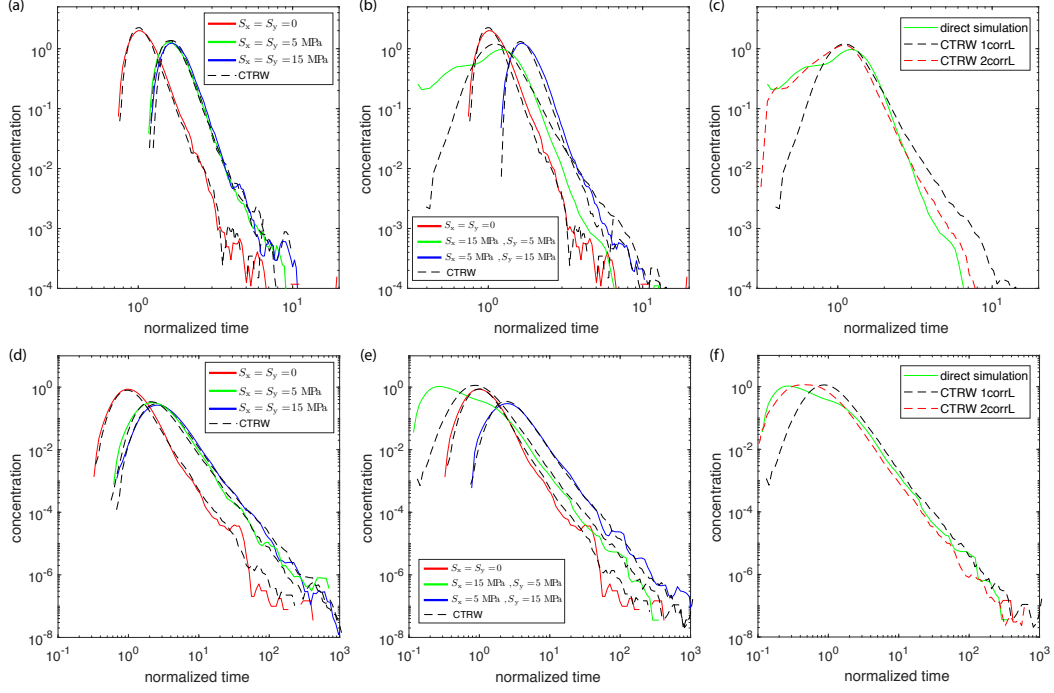


Figure 16. BTCs from direct numerical simulations (solid line) and model predictions (dashed line). Tracer arrival times are normalized with the peak arrival time of the zero stress loading case. (a) BTC predictions for isotropic stress conditions with constant initial aperture. (b) BTC predictions for anisotropic stress conditions with constant initial aperture. (c) The model predictions for $S_x = 15$ MPa and $S_y = 5$ MPa case with constant initial aperture. The prediction with dual correlation length shows improved prediction. (d) BTCs predictions for isotropic stress conditions with variable initial aperture. (e) BTCs predictions for anisotropic stress conditions with variable initial aperture. (f) The model predictions for $S_x = 15$ MPa and $S_y = 5$ MPa case with variable initial aperture. The prediction with dual correlation length shows improved prediction.

The key observations made in this study are indeed consistent with previous laboratory experiments and field studies. First, the observed response of the fracture network with respect to the stress magnitude is consistent with laboratory studies that showed the reduction in fracture permeability with the increase in normal stress (N. Barton et al., 1985; Pyrak-Nolte & Morris, 2000; Y. W. Tsang & Witherspoon, 1981), and field observations that showed the decrease in rock permeability with the increase of formation depth (Achtziger-Zupančič, Loew, & Mariéthoz, 2017; Rutqvist, 2015; Rutqvist & Stephansson, 2003). Second, the significant shear dilation of the preferentially-oriented fractures is consistent with laboratory studies that have shown an increase in fracture permeability due to shear-induced dilation (Lee & Cho, 2002; Olsson & Barton, 2001; Yeo, de Freitas, & Zimmerman, 1998), and field observations that have shown that only a small proportion of fractures are conductive (Follin et al., 2014; C.-F. Tsang & Neretnieks, 1998) due to the associated critically stressed state (C. A. Barton, Zoback, & Moos, 1995). Shear dilation as a means of enhancing permeability of naturally fractured reservoirs to stimulate production has also been recognized by geothermal and petroleum industries (Deichmann & Giardini, 2009; Evans et al., 1999; Rahman, Hossain, & Rahman, 2002). However, most of the existing laboratory and field studies on stress effects are limited to fluid flow measurements. Therefore, experimental studies involving transport measurements are much needed.

The effects of geological stress on particle transport are apparent from the space-Lagrangian velocity statistics that determine tracer transport. For constant initial aperture cases, the increase in the stress magnitude simply translates velocity distributions towards low velocity values and does not impact effective tracer spreading behavior. The emergence of fast velocities is observed only in the case with $S_x = 15$ MPa and $S_y = 5$ MPa. This is due to the shear-dilation-induced preferential flow paths. For variable initial aperture cases, geological stress has a dramatic impact on both early and late-time arrival of tracers. An increase in the stress magnitude significantly broadens velocity distributions towards small velocities and also changes the scaling of small velocities. For the case with $S_x = 15$ MPa and $S_y = 5$ MPa, we clearly observe the emergence of both large velocities and small velocities. Lagrangian velocity correlation lengths are not very sensitive to geological stress conditions except for the $S_x = 15$ MPa and $S_y = 5$ MPa case. In this case, preferential paths induced by shear-dilation significantly increase velocity correlation lengths for high velocities. The effect of preferential paths is also apparent from the decreased tortuosity for $S_x = 15$ MPa and $S_y = 5$ MPa case.

We have presented the Bernoulli CTRW model that incorporates the essential features of the space-Lagrangian velocity statistics. The model is shown to successfully capture anoma-

lous transport in natural fracture networks under various stress conditions. The model with a single effective velocity correlation length accurately captures tracer breakthrough curves except for the $S_x = 15$ MPa and $S_y = 5$ MPa case. The agreement between model predictions and direct numerical simulations indicates that the simple velocity correlation model can capture the dominant velocity correlation structure in natural fracture networks unless there is a strong channeling caused by shear dilation. We extended the velocity correlation model to have dual correlation lengths: one for the fast, correlated velocities and the other for less correlated velocities. The dual correlation length model was shown to capture effective spreading behavior of the $S_x = 15$ MPa and $S_y = 5$ MPa case. The anomalously early arrival is caused by spatially correlated fast flow paths, and late-time tailing is caused by the emergence of small velocities that are spatially randomly distributed. This gives two distinct velocity correlation lengths, which is confirmed from the conditional velocity correlation functions.

Applying this modeling framework in the field requires the PDF of the Eulerian velocity magnitude (a flow attribute) and the velocity correlation as inputs, which are often not available a priori. However, the model can indeed also be parameterized from available field data such as tracer breakthrough curves (Kang, Le Borgne, et al., 2015), which can be used to estimate the parameters in a functional approximation of the velocity PDF. Regarding the correlation length, the effective transport behavior can be predicted based on a single (average) correlation length in many situations (Kang et al., 2017; Kang, Le Borgne, et al., 2015; Puyguiraud, Gouze, & Dentz, 2019).

This study highlights the critical importance of incorporating geomechanical analysis in DFN simulations in order to more accurately derive aperture distributions and model flow and transport processes. The conventional approaches that neglect the effects of geological stress state may lead to an underestimation of aperture heterogeneity and flow channelization. The findings in this study have important implications for many subsurface technologies. For example, fractured rocks around nuclear waste disposal sites can be under strongly anisotropic stress loadings such that some preferentially-oriented fractures may establish preferential pathways for radionuclide migration—an effect that cannot be predicted without considering the geomechanical effects. The coupled geomechanics–flow–transport analysis would also help improve the design of fractured aquifer remediation strategies by more precisely predicting the contaminant transport in geologically stressed heterogeneous fractured media. The topic of coupled stress-flow-transport is not only critical for the subsurface technologies but also for natural processes such as topographic stress-controlled bedrock weathering. Topographic and tectonic-

stress-induced fractures are known to be one of the dominant mechanisms for the deep critical zone weathering (Clair et al., 2015; Riebe, Hahm, & Brantley, 2017). The modeling framework in this study can be extended to study how tectonics influence deep critical zone architecture.

Like any modeling work, this study is based on assumptions that conceptualize the problem. First, this work did not consider matrix diffusion. This should not affect our main conclusions for the Bristol Channel since the effects of matrix diffusion on transport is negligible (Edery et al., 2016). However, this is not necessarily true for all geological settings. In addition, this work studied 2D fracture system, and there could be important 3D effects. While several studies have investigated fluid flow in stressed 3D fracture networks (Garipov, Karimi-Fard, & Tchelepi, 2016; Lei, Wang, et al., 2017; McClure, Babazadeh, Shiozawa, & Huang, 2016), the effects of geological stress on tracer transport through 3D fracture networks remain to be investigated. A recent study has shown that the Bernoulli CTRW model can capture particle transport through 3D fracture networks (J. D. Hyman et al., 2019), and the natural extension of this study will be the effects of geological stress on particle transport through *stressed* 3D fracture networks. Finally, since fracture network properties and *in-situ* stress conditions can vary widely from location to location, additional studies are required to obtain more general conclusions.

Acknowledgments

PKK acknowledges the College of Science & Engineering at the University of Minnesota and the George and Orpha Gibson Endowment for its generous support of Hydrogeology. PKK also acknowledges a grant from Korea Environment Industry & Technology Institute (KEITI) through Subsurface Environmental Management (SEM) Project, funded by Korea Ministry of Environment (MOE) W12530(2018002440003). MD acknowledges the support of the European Research Council (ERC) through the project MHetScale (617511). RJ acknowledges funding by the US Department of Energy Office of Science (grant number DE-SC0018357). The digitized Bristol fracture network data is freely available through a data repository system at the University of Minnesota (<https://doi.org/10.13020/ah7v-6n67>).

References

Achtziger-Zupančič, P., Loew, S., & Mariéthoz, G. (2017). A new global database to improve predictions of permeability distribution in crystalline rocks at site scale. *J. Geo-*

- phys. Res. Solid Earth*, 122(5), 3513–3539.
- Baghbanan, A., & Jing, L. (2008). Stress effects on permeability in a fractured rock mass with correlated fracture length and aperture. *Int. J. Rock Mech. Min. Sci.*, 45(8), 1320–1334.
- Bandis, S., Lumsden, A. C., & Barton, N. R. (1981). Experimental studies of scale effects on the shear behaviour of rock joints. *Int. J. Rock Mech. Min. Sci. Geomech. Abstr.*, 18(1), 1–21.
- Bandis, S., Lumsden, A. C., & Barton, N. R. (1983). Fundamentals of rock joint deformation. *Int. J. Rock Mech. Min. Sci. Geomech. Abstr.*, 20(6), 249–268.
- Barton, C. A., Zoback, M. D., & Moos, D. (1995). Fluid flow along potentially active faults in crystalline rock. *Geology*, 23(8), 683–686.
- Barton, N., Bandis, S., & Bakhtar, K. (1985). Strength, deformation and conductivity coupling of rock joints. *Int. J. Rock Mech. Min. Sci. Geomech. Abstr.*, 22(3), 121–140.
- Barton, N., & Choubey, V. (1977). The shear strength of rock joints in theory and practice. *Rock Mech.*, 10(1-2), 1–54.
- Belayneh, M. (2004). Palaeostress orientation inferred from surface morphology of joints on the southern margin of the Bristol Channel Basin, UK. *Geol. Soc. London, Spec. Publ.*, 231(1), 243–255.
- Belayneh, M., & Cosgrove, J. W. (2004). Fracture-pattern variations around a major fold and their implications regarding fracture prediction using limited data: an example from the Bristol Channel Basin. *Geol. Soc. London Spec. Publ.*, 231(1), 89–102.
- Benedetto, M. F., Berrone, S., Borio, A., Pieraccini, S., & Scialò, S. (2016). A hybrid mortar virtual element method for discrete fracture network simulations. *J. Comput. Phys.*, 306, 148–166.
- Berkowitz, B., & Scher, H. (1997). Anomalous transport in random fracture networks. *Phys. Rev. Lett.*, 79(20), 4038.
- Bijeljic, B., Mostaghimi, P., & Blunt, M. J. (2011). Signature of non-Fickian solute transport in complex heterogeneous porous media. *Phys. Rev. Lett.*, 107, 204502.
- Bolster, D., Méheust, Y., Le Borgne, T., Bouquain, J., & Davy, P. (2014). Modeling preasymptotic transport in flows with significant inertial and trapping effects—the importance of velocity correlations and a spatial markov model. *Adv. Water Resour.*, 70, 89–103.
- Bonnet, E., Bour, O., Odling, N. E., Davy, P., Mainn, I., Cowie, P., & Berkowitz, B. (2001).

- Scaling of fracture systems in geological media. *Rev. Geophys.*, 39(3), 347–383.
- Cacas, M. C., Ledoux, E., de Marsily, G., Barbreau, A., Calmels, P., Gaillard, B., & Margritta, R. (1990). Modeling fracture flow with a stochastic discrete fracture network: Calibration and validation: 2. The transport model. *Water Resour. Res.*, 26(3), 491–500.
- Cacas, M. C., Ledoux, E., Marsily, G., Tillie, B., Barbreau, A., Durand, E., ... Peaudecerf, P. (1990). Modeling fracture flow with a stochastic discrete fracture network: calibration and validation: 1. The flow model. *Water Resour. Res.*, 26(3), 479–489.
- Cardenas, M. B., Slotke, D. T., Ketcham, R. A., & Sharp, J. M. (2007). Navier-Stokes flow and transport simulations using real fractures shows heavy tailing due to eddies. *Geophys. Res. Lett.*, 34(14), L14404.
- Clair, J. S., Moon, S., Holbrook, W., Perron, J., Riebe, C., Martel, S., ... others (2015). Geophysical imaging reveals topographic stress control of bedrock weathering. *Science*, 350(6260), 534–538.
- de Dreuzy, J.-R., Davy, P., & Bour, O. (2001). Hydraulic properties of two-dimensional random fracture networks following a power law length distribution: 2. Permeability of networks based on lognormal distribution of apertures. *Water Resour. Res.*, 37(8), 2079–2095.
- Deichmann, N., & Giardini, D. (2009). Earthquakes induced by the stimulation of an enhanced geothermal system below Basel (Switzerland). *Seismol. Res. Lett.*, 80(5), 784–798.
- Dentz, M., Kang, P. K., Comolli, A., Le Borgne, T., & Lester, D. R. (2016). Continuous time random walks for the evolution of Lagrangian velocities. *Phys. Fluids*, 1(7), 074004.
- Dverstorp, B., & Andersson, J. (1989). Application of the discrete fracture network concept with field data: Possibilities of model calibration and validation. *Water Resour. Res.*, 25(3), 540–550.
- Edery, Y., Geiger, S., & Berkowitz, B. (2016). Structural controls on anomalous transport in fractured porous rock. *Water Resour. Res.*, 52(7), 5634–5643.
- Evans, K. F., Cornet, F. H., Hashida, T., Hayashi, K., Ito, T., Matsuki, K., & Wallroth, T. (1999). Stress and rock mechanics issues of relevance to HDR/HWR engineered geothermal systems: review of developments during the past 15 years. *Geothermics*, 28(4–5), 455–474.
- Figueiredo, B., Tsang, C.-F., Rutqvist, J., & Niemi, A. (2015). A study of changes in deep

- fractured rock permeability due to coupled hydro-mechanical effects. *Int. J. Rock Mech. Min. Sci.*, 79, 70–85.
- Follin, S., Hartley, L., Rhén, I., Jackson, P., Joyce, S., Roberts, D., & Swift, B. (2014). A methodology to constrain the parameters of a hydrogeological discrete fracture network model for sparsely fractured crystalline rock, exemplified by data from the proposed high-level nuclear waste repository site at Forsmark, Sweden. *Hydrogeol. J.*, 22(2), 313–331.
- Garabedian, S. P., LeBlond, D. R., Gelhar, L. W., & Celia, M. A. (1991). Large-scale natural gradient tracer test in sand and gravel, Cape Cod, Massachusetts 2. Analysis of spatial moments for a nonreactive tracer. *Water Resour. Res.*, 27(5), 911–924.
- Garipov, T. T., Karimi-Fard, M., & Tchelepi, H. A. (2016). Discrete fracture model for coupled flow and geomechanics. *Comput. Geosci.*, 20(1), 149–160.
- Geiger, S., Cortis, A., & Birkholzer, J. (2010). Upscaling solute transport in naturally fractured porous media with the continuous time random walk method. *Water Resour. Res.*, 46(12), W12530.
- Geiger, S., & Emmanuel, S. (2010). Non-Fourier thermal transport in fractured geological media. *Water Resour. Res.*, 46(7), W07504.
- Huseby, O., Thovert, J.-F., & Adler, P. (2001). Dispersion in three-dimensional fracture networks. *Phys. Fluids*, 13(3), 594–615.
- Hyman, J., & Jiménez-Martínez, J. (2018). Dispersion and mixing in three-dimensional discrete fracture networks: Nonlinear interplay between structural and hydraulic heterogeneity. *Water Resour. Res.*, 54, 3243–3258.
- Hyman, J. D., Dentz, M., Hagberg, A., & Kang, P. K. (2019). Linking structural and transport properties in three-dimensional fracture networks. *J. Geophys. Res. Solid Earth*.
- Jing, L., Min, K. B., Baghbanan, A., & Zhao, Z. (2013). Understanding coupled stress, flow and transport processes in fractured rocks. *Geosyst. Eng.*, 16(1), 2–25.
- Juanes, R., Samper, J., & Molinero, J. (2002). A general and efficient formulation of fractures and boundary conditions in the finite element method. *Int. J. Numer. Meth. Eng.*, 54(12), 1751–1774.
- Kandhai, D., Hlushkou, D., Hoekstra, A. G., Soot, P. M. A., As, H. V., & Tallarek, U. (2002). Influence of stagnant zones on transient and asymptotic dispersion in macroscopically homogeneous porous media. *Phys. Rev. Lett.*, 88, 234501.
- Kang, P. K., Brown, S., & Juanes, R. (2016). Emergence of anomalous transport in stressed

- rough fractures. *Earth Planet. Sci. Lett.*, 454, 46–54.
- Kang, P. K., de Anna, P., Nunes, J. P., Bijeljic, B., Blunt, M. J., & Juanes, R. (2014). Pore-scale intermittent velocity structure underpinning anomalous transport through 3-D porous media. *Geophys. Res. Lett.*, 41(17), 6184–6190.
- Kang, P. K., Dentz, M., Le Borgne, T., & Juanes, R. (2015). Anomalous transport on regular fracture networks: Impact of conductivity heterogeneity and mixing at fracture intersections. *Phys. Rev. E*, 92(2), 022148.
- Kang, P. K., Dentz, M., Le Borgne, T., Lee, S., & Juanes, R. (2017). Anomalous transport in disordered fracture networks: spatial markov model for dispersion with variable injection modes. *Adv. Water Resour.*, 106, 80–94.
- Kang, P. K., Le Borgne, T., Dentz, M., Bour, O., & Juanes, R. (2015). Impact of velocity correlation and distribution on transport in fractured media: Field evidence and theoretical model. *Water Resour. Res.*, 51(2), 940–959.
- Koudina, N., Garcia, R. G., Thovert, J.-F., & Adler, P. (1998). Permeability of three-dimensional fracture networks. *Phys. Rev. E*, 57(4), 4466.
- Lama, R. D., & Vutukuri, V. S. (1978). *Handbook on mechanical properties of rocks: Testing techniques and results (vol. 2)*. Trans. Tech. Publications.
- Latham, J.-P., Xiang, J., Belayneh, M., Nick, H., Tsang, C.-F., & Blunt, M. J. (2013). Modelling stress-dependent permeability in fractured rock including effects of propagating and bending fractures. *Int. J. Rock Mech. Min. Sci.*, 57, 100–112.
- Le Borgne, T., de Dreuzay, J.-R., Davy, P., & Bour, O. (2007). Characterization of the velocity field organization in heterogeneous media by conditional correlation. *Water Resour. Res.*, 43(2), W02419.
- Le Borgne, T., Dentz, M., & Carrera, J. (2008). Spatial markov processes for modeling lagrangian particle dynamics in heterogeneous porous media. *Phys. Rev. E*, 78(2), 026308.
- Le Borgne, T., & Gouze, P. (2007). Non-Fickian dispersion in porous media: 2. Model validation from measurements at different scales. *Water Resour. Res.*, 44, W06427.
- Lee, H. S., & Cho, T. F. (2002). Hydraulic characteristics of rough fractures in linear flow under normal and shear load. *Rock Mech. Rock Eng.*, 35(4), 299–318.
- Lei, Q., & Gao, K. (2018). Correlation between fracture network properties and stress variability in geological media. *Geophys. Res. Lett.*, 45(9), 3994–4006.
- Lei, Q., Latham, J.-P., & Tsang, C.-F. (2017). The use of discrete fracture networks for mod-

- elling coupled geomechanical and hydrological behaviour of fractured rocks. *Comput. Geotech.*, 85, 151-176.
- Lei, Q., Latham, J.-P., & Xiang, J. (2016). Implementation of an empirical joint constitutive model into finite-discrete element analysis of the geomechanical behaviour of fractured rocks. *Rock Mech. Rock Eng.*, 49(12), 4799–4816.
- Lei, Q., Latham, J.-P., Xiang, J., Tsang, C.-F., Lang, P., & Guo, L. (2014). Effects of geomechanical changes on the validity of a discrete fracture network representation of a realistic two-dimensional fractured rock. *Int. J. Rock Mech. Min. Sci.*, 70, 507–523.
- Lei, Q., Wang, X., Xiang, J., & Latham, J.-P. (2017). Polyaxial stress-dependent permeability of a three-dimensional fractured rock layer. *Hydrogeol. J.*, 25(8), 2251-2262.
- Levy, M., & Berkowitz, B. (2003). Measurement and analysis of non-Fickian dispersion in heterogeneous porous media. *J. Contaminant Hydrol.*, 64, 203–226.
- Liu, R., Li, B., Jiang, Y., & Yu, L. (2018). A numerical approach for assessing effects of shear on equivalent permeability and nonlinear flow characteristics of 2-D fracture networks. *Adv. Water Resour.*, 111, 289–300.
- Long, J. C. S., & Billaux, D. M. (1987). From field data to fracture network modeling: An example incorporating spatial structure. *Water Resour. Res.*, 23(7), 1201-1216.
- Ma, G., Wang, Y., Li, T., & Chen, Y. (2019). A mesh mapping method for simulating stress-dependent permeability of three-dimensional discrete fracture networks in rocks. *Comput. Geotech.*, 108, 95–106.
- Maillot, J., Davy, P., Le Goc, R., Darcel, C., & De Dreuzy, J.-R. (2016). Connectivity, permeability, and channeling in randomly distributed and kinematically defined discrete fracture network models. *Water Resour. Res.*, 52(11), 8526–8545.
- Makedonska, N., Painter, S. L., Bui, Q. M., Gable, C. W., & Karra, S. (2015). Particle tracking approach for transport in three-dimensional discrete fracture networks. *Computat. Geosci.*, 19(5), 1123–1137.
- Matthäi, S. K., & Belayneh, M. (2004). Fluid flow partitioning between fractures and a permeable rock matrix. *Geophys. Res. Lett.*, 31, L07602.
- Matthäi, S. K., Nick, H. M., Pain, C., & Neuweiler, I. (2010). Simulation of solute transport through fractured rock: a higher-order accurate finite-element finite-volume method permitting large time steps. *Transport Porous Med.*, 83(2), 289–318.
- McClure, M. W., Babazadeh, M., Shiozawa, S., & Huang, J. (2016). Fully coupled hydromechanical simulation of hydraulic fracturing in 3d discrete-fracture networks. *SPE Jour-*

- nal*, 21(04), 1302–1320.
- Min, K.-B., Rutqvist, J., Tsang, C.-F., & Jing, L. (2004). Stress-dependent permeability of fractured rock masses: a numerical study. *Int. J. Rock Mech. Min. Sci.*, 41, 1191–1210.
- Molinero, J., Samper, J., & Juanes, R. (2002). Numerical modeling of the transient hydrogeological response produced by tunnel construction in fractured bedrocks. *Eng. Geol.*, 64(4), 369–386.
- Moroni, M., Kleinfelter, N., & Cushman, J. H. (2007). Analysis of dispersion in porous media via matched-index particle tracking velocimetry experiments. *Adv. Water Resour.*, 30(1), 1–15.
- Munjiza, A. (2004). *The combined finite-discrete element method*. London: Wiley.
- Neuman, S. P., & Di Federico, V. (2003). Multifaceted nature of hydrogeologic scaling and its interpretation. *Rev. Geophys.*, 41(3).
- Nick, H. M., Paluszny, A., Blunt, M. J., & Matthäi, S. K. (2011). Role of geomechanically grown fractures on dispersive transport in heterogeneous geological formations. *Phys. Rev. E*, 84, 056301.
- Oda, M. (1986). An equivalent continuum model for coupled stress and fluid flow analysis in jointed rock masses. *Water Resour. Res.*, 22(13), 1845–1856.
- Olsson, R., & Barton, N. (2001). An improved model for hydromechanical coupling during shearing of rock joints. *Int. J. Rock Mech. Min. Sci.*, 38(3), 317–329.
- Paluszny, A., & Matthai, S. K. (2010). Impact of fracture development on the effective permeability of porous rocks as determined by 2-D discrete fracture growth modeling. *J. Geophys. Res.*, 115(B2), B02203.
- Park, Y.-J., de Dreuzy, J.-R., Lee, K.-K., & Berkowitz, B. (2001). Transport and intersection mixing in random fracture networks with power law length distributions. *Water Resour. Res.*, 37(10), 2493–2501.
- Porta, G. M., Bijeljic, B., Blunt, M. J., & Guadagnini, A. (2015). Continuum-scale characterization of solute transport based on pore-scale velocity distributions. *Geophys. Res. Lett.*, 42(18), 7537–7545.
- Puyguraud, A., Gouze, P., & Dentz, M. (2019). Stochastic dynamics of Lagrangian pore-scale velocities in three-dimensional porous media. *Water Resour. Res.*, 55(2), 1196–1217.
- Pyrak-Nolte, L. J., Montemagno, C. D., & Nolte, D. D. (1997). Volumetric imaging of aper-

- ture distributions in connected fracture networks. *Geophys. Res. Lett.*, 24(18), 2343–2346.
- Pyrak-Nolte, L. J., & Morris, J. P. (2000). Single fractures under normal stress: The relation between fracture specific stiffness and fluid flow. *Int. J. Rock Mech. Min. Sci.*, 37(1-2), 245–262.
- Rahman, M. K., Hossain, M. M., & Rahman, S. S. (2002). A shear-dilation-based model for evaluation of hydraulically stimulated naturally fractured reservoirs. *Int. J. Numer. Anal. Methods Geomech.*, 26(5), 469–497.
- Raven, K. G., & Gale, J. E. (1985). Water flow in a natural rock fracture as a function of stress and sample size. In *Int. j. rock mech. min. sci. geomech. abstr.* (Vol. 22, pp. 251–261).
- Riebe, C. S., Hahm, W. J., & Brantley, S. L. (2017). Controls on deep critical zone architecture: A historical review and four testable hypotheses. *Earth Surf. Proc. Land.*, 42(1), 128–156.
- Risken, H. (1996). *The Fokker-Planck equation*. Heidelberg, New York: Springer.
- Rutqvist, J. (2015). Fractured rock stress-permeability relationships from in situ data and effects of temperature and chemical-mechanical couplings. *Geofluids*, 15(1-2), 48–66.
- Rutqvist, J., Leung, C., Hoch, A., Wang, Y., & Wang, Z. (2013). Linked multicontinuum and crack tensor approach for modeling of coupled geomechanics, fluid flow and transport in fractured rock. *J. Rock Mech. Geotech. Eng.*, 5(1), 18–31.
- Rutqvist, J., & Stephansson, O. (2003). The role of hydromechanical coupling in fractured rock engineering. *Hydrogeol. J.*, 11(1), 7–40.
- Scheven, U. M., Verganelakis, D., Harris, R., Johns, M. L., & Gladden, L. F. (2005). Quantitative nuclear magnetic resonance measurements of preasymptotic dispersion in flow through porous media. *Phys. Fluids*, 17, 117107.
- Sherman, T., Hyman, J. D., Bolster, D., Makedonska, N., & Srinivasan, G. (2019). Characterizing the impact of particle behavior at fracture intersections in three-dimensional discrete fracture networks. *Phys. Rev. E*, 99(1), 013110.
- Snow, D. T. (1970). The frequency and apertures of fractures in rock. In (Vol. 7, pp. 23–40).
- Sund, N. L., Bolster, D., & Benson, D. A. (2016). Testing the limits of the spatial Markov model for upscaling transport: The role of nonmonotonic effective velocity autocorrelations. *Phys. Rev. E*, 94(4), 043107.
- Tsang, C.-F. (1991). Coupled hydromechanical-thermochemical processes in rock fractures.

- Rev. Geophys.*, 29(4), 537–551.
- Tsang, C.-F., & Neretnieks, I. (1998). Flow channeling in heterogeneous fractured rocks. *Rev. Geophys.*, 36(2), 275–298.
- Tsang, Y. W., & Witherspoon, P. A. (1981). Hydromechanical behavior of a deformable rock fracture subject to normal stress. *J. Geophys. Res. Solid Earth*, 86(B10), 9287–9298.
- Viswanathan, H. S., Hyman, J. D., Karra, S., O'Malley, D., Srinivasan, S., Hagberg, A., & Srinivasan, G. (2018). Advancing graph-based algorithms for predicting flow and transport in fractured rock. *Water Resour. Res.*, 54(9), 6085–6099.
- Wang, L., & Cardenas, M. B. (2014). Non-Fickian transport through two-dimensional rough fractures: Assessment and prediction. *Water Resour. Res.*, 50(2), 871–884.
- Wang, Z., Rutqvist, J., Wang, Y., Leung, C., Hoch, A., & Dai, Y. (2014). The effect of stress on flow and transport in fractured rock masses using an extended multiple interacting continua method with crack tensor theory. *Nucl. Technol.*, 187(2), 158–168.
- Willmann, M., Lanyon, G. W., Marschall, P., & Kinzelbach, W. (2013). A new stochastic particle-tracking approach for fractured sedimentary formations. *Water Resour. Res.*, 49(1), 352–359.
- Witherspoon, P. A., Wang, J. S., Iwai, K., & Gale, J. E. (1980). Validity of cubic law for fluid flow in a deformable rock fracture. *Water Resour. Res.*, 16(6), 1016–1024.
- Yeo, I. W., de Freitas, M. H., & Zimmerman, R. W. (1998). Effect of shear displacement on the aperture and permeability of a rock fracture. *Int. J. Rock Mech. Min. Sci.*, 35(8), 1051–1070.
- Zhang, X., & Sanderson, D. J. (1996). Effects of stress on the two-dimensional permeability tensor of natural fracture networks. *Geophys. J. Int.*, 125(3), 912–924.
- Zhao, Z., Jing, L., & Neretnieks, I. (2010). Evaluation of hydrodynamic dispersion parameters in fractured rocks. *J. Rock Mech. Geotech. Eng.*, 2(3), 243–254.
- Zhao, Z., Jing, L., Neretnieks, I., & Moreno, L. (2011). Numerical modeling of stress effects on solute transport in fractured rocks. *Comput. Geotech.*, 38(2), 113–126.
- Zhao, Z., Rutqvist, J., Leung, C., Hokr, M., Liu, Q., Neretnieks, I., . . . Zimmerman, R. (2013). Impact of stress on solute transport in a fracture network: a comparison study. *J. Rock Mech. Geotech. Eng.*, 5(2), 110–123.
- Zoback, M. L. (1992). First- and second-order patterns of stress in the lithosphere: The world stress map project. *J. Geophys. Res. Solid Earth*, 97(B8), 11703–11728.